

AperTO - Archivio Istituzionale Open Access dell'Università di Torino

From biogenic silica and organic matter to authigenic clays and dolomite: Insights from Messinian (upper Miocene) sediments of the Northern Mediterranean

This is a pre print version of the following article:

Original Citation:

Availability:

This version is available <http://hdl.handle.net/2318/1883027> since 2025-02-19T11:27:14Z

Published version:

DOI:10.1111/sed.13053

Terms of use:

Open Access

Anyone can freely access the full text of works made available as "Open Access". Works made available under a Creative Commons license can be used according to the terms and conditions of said license. Use of all other works requires consent of the right holder (author or publisher) if not exempted from copyright protection by the applicable law.

(Article begins on next page)

Pellegrino Luca (Orcid ID: 0000-0003-2762-9821)
Natalicchio Marcello (Orcid ID: 0000-0002-8309-3075)
Peckmann Jörn (Orcid ID: 0000-0002-8572-0060)

From biogenic silica and organic matter to authigenic clays and dolomite: Insights from Messinian (upper Miocene) sediments of the Northern Mediterranean

Luca Pellegrino*¹, Marcello Natalicchio¹, Daniel Birge², Linda Pastero¹, Giorgio Carnevale¹,
Richard W. Jordan³, Jörn Peckmann², Nicolò Zanellato¹, Francesco Dela Pierre¹

¹Dipartimento di Scienze della Terra, Università degli Studi di Torino, Via Valperga Caluso 35, 10125 Torino, Italy

²Institut für Geologie, Centrum für Erdsystemforschung und Nachhaltigkeit, Universität Hamburg, 20146 Hamburg, Germany

³Faculty of Science, Yamagata University, 990-8560 Yamagata, Japan

*Corresponding author: lu.pellegrino@unito.it

Associate Editor – Mike Rogerson

Short Title – Messinian authigenic clays and dolomite

ABSTRACT

The biogeochemical cycles of carbon and silicon are tightly coupled in modern marine environments due to the pivotal role of planktonic diatoms. Once diatoms are sedimented, the fate of organic matter and biogenic silica is initially governed by bottom water oxygen levels and bacterial communities involved in remineralization processes. The early diagenesis of biosiliceous sediments may result in drastic changes in composition, sometimes hampering palaeoenvironmental reconstruction. Sedimentary successions deposited in the Mediterranean region during the Messinian salinity crisis (5.97 – 5.33 Ma) allow to explore the early diagenetic transformation of organic matter and biogenic silica in a restricted basin experiencing a severe palaeoceanographic turnover. Sedimentological and petrographic observations coupled to elemental, mineralogical,

This article has been accepted for publication and undergone full peer review but has not been through the copyediting, typesetting, pagination and proofreading process which may lead to differences between this version and the [Version of Record](#). Please cite this article as doi: [10.1111/sed.13053](https://doi.org/10.1111/sed.13053)

This article is protected by copyright. All rights reserved.

inorganic and organic geochemical analyses were carried out on biosiliceous (diatomaceous shales and diatom-bearing mudstones) and associated clay-rich and dolomite-rich sediments (dolomitic mudstones) interbedded with primary gypsum layers in the Piedmont Basin (north-west Italy). The state of preservation of biogenic silica was governed by different pathways of organic matter remineralization, depending on bottom and pore water redox conditions, which were controlled by the structure of the water column. Aerobic respiration of organic matter in a mixed water column and an oxygenated seafloor promoted biogenic silica preservation. In contrast, bottom water anoxia induced by permanent stratification of the water column favoured the concomitant formation of dolomite and authigenic clays. In particular, organic matter degradation through bacterial sulphate reduction increased pore water alkalinity, promoting the precipitation of dolomite. At the same time, the rise in pH promoted the dissolution of biogenic silica which, reacting with pore water cations, ultimately caused the formation of authigenic clays. This study suggests that the apparent annihilation of Mediterranean marine biota during the Messinian salinity crisis partially reflects an early diagenetic bias produced by interactions of the carbon, silicon and sulphur biogeochemical cycles in a restricted basin.

Key-words: authigenic clays, biogenic silica, dolomite; early diagenesis, lipid biomarkers, Messinian salinity crisis, organic matter.

INTRODUCTION

In modern oceans silica-secreting microorganisms play a fundamental role in the biogeochemical cycles of carbon (C) and silicon (Si) (Tréguer *et al.*, 2018, 2021). Notably, planktonic diatoms account for approximately 40% of marine primary production and dominate the pelagic production of biogenic silica, exporting around 0.1 to 0.2 Gt C and 3.1 Gt Si from surface waters each year (Pierella Karlusich *et al.*, 2021; Tréguer *et al.*, 2021). Both C and Si are subjected

to various degrees of diagenetic transformation immediately after deposition at ambient conditions (e.g. Michalopoulos & Aller, 2004), and during burial following significant temperature change depending on depth and local geothermal gradient (e.g. van der Lingen, 1977). Addressing diagenetic processes is therefore pivotal for constraining the biogeochemical cycles of C and Si since diagenetic alteration may compromise the reconstruction of palaeoenvironments and the study of evolutionary trajectories of siliceous microorganisms – both potentially biased by the sequential loss of biomineralized remains in the sedimentary record (e.g. Cermeño, 2016; Westacott *et al.*, 2021). Several studies have demonstrated a fundamental contribution of diatoms and other siliceous organisms to the accumulation of organic matter in sediments, even in cases where biogenic silica is scarce or no longer preserved (e.g. Sinninghe Damsté *et al.*, 1995; Schulz *et al.*, 1996; Dickman & Glenwright, 1997; Kemp *et al.*, 1998, 1999; Pearce *et al.*, 1998; Schwark *et al.*, 2009; McKirdy *et al.*, 2013; Isaji *et al.*, 2019; Elling *et al.*, 2021).

While burial diagenesis of biosiliceous sediments has already been studied extensively (e.g. van der Lingen, 1977; Hein *et al.*, 1978; Pisciotto, 1981; Behl & Garrison, 1994; Thyberg *et al.*, 1999; Davies & Cartwright, 2002; Abu-Mahfouz *et al.*, 2020; Varkouhi *et al.*, 2021), the early diagenetic transformation and degradation pathways involving biogenic silica and organic matter at the sediment–water interface and in the topmost part of the sedimentary column are less well constrained (e.g. Michalopoulos & Aller, 1995, 2004). Organic matter associated with cells of siliceous microorganisms can be degraded aerobically (e.g. Holstein & Hensen, 2009; Jørgensen *et al.*, 2022), leaving no direct mineralogical evidence in the rock record if diatom frustules are dissolved. In contrast, bottom water anoxia favours bacterial organoclastic sulphate reduction (i.e. sulphate reduction with organic matter as electron donor). Sulphate reduction commonly causes the formation of authigenic carbonate – especially dolomite – and iron sulphide (pyrite) minerals by the generation of alkalinity and more reducing conditions (e.g. Vasconcelos *et al.*, 1995; Wilkin *et al.*, 1996; Wright, 1999; Mazzullo, 2000; Warren, 2000; Shoonen, 2004; Wright & Wacey, 2005; Bontognali *et al.*, 2010, 2013; Zhang *et al.*, 2012; Petrash *et al.*, 2017; Lu *et al.*, 2018; Duverger *et*

al., 2020; Li *et al.*, 2021; Tribovillard *et al.*, 2022). Such microbially-produced mineral phases provide evidence of formerly high contents of organic matter in the sediments, even if organic matter is no longer preserved.

The early diagenesis of biogenic silica in modern sediments has been addressed mainly by numerical model calculations based on the chemical analysis of pore water (e.g. Tréguer *et al.*, 2021), with few studies focusing on mineralogical aspects of this process (e.g. Michalopoulos & Aller, 1995, 2004). Interestingly, biogenic silica alteration in combination with free cation-rich pore waters promotes authigenic clay formation (a reaction known as reverse weathering), which is a fast process potentially representing an underestimated sink of Si (e.g. Badaut & Risacher, 1983; Noël & Rouchy, 1986; Michalopoulos and Aller, 1995, 2004; Presti & Michalopoulos, 2008; Rahman, 2019). Several studies demonstrated that authigenic clay formation can be microbially-mediated, highlighting the close interplay of the C and Si biogeochemical cycles during early diagenesis (e.g. Konhauser & Urrutia, 1999; Kim *et al.*, 2004, 2019; Liu *et al.*, 2012; Bontognali *et al.*, 2014; Burne *et al.*, 2014; Kremer *et al.*, 2018, 2019; del Buey *et al.*, 2021).

This paper presents the results of a combined sedimentological, petrographic, mineralogical and geochemical study of biogenic silica-rich, dolomite-rich and clay-rich deposits formed during the so-called Messinian salinity crisis (MSC), a major palaeoceanographic event that affected the Mediterranean in the late Neogene, between 5.97 and 5.33 Ma (Ryan, 1973; Selli, 1973; Hsü *et al.*, 1973; Cita *et al.*, 1978; Krijgsman *et al.*, 1999; Rouchy & Caruso, 2006; Roveri *et al.*, 2014). This event was associated with the formation of more than 1 million km³ of evaporites (carbonate minerals, gypsum and halite; Haq *et al.*, 2020) in both peripheral marginal basins and deep basinal areas. Many evaporites are rhythmically interbedded with clay-rich and dolomite-rich layers. The lithologies consisting of non-evaporite minerals have received much less attention than the evaporites themselves, although their study can provide valuable insights for palaeoenvironmental reconstructions (e.g. Dela Pierre *et al.*, 2014). This study focuses on a sedimentary succession deposited during the first stage of the MSC in the Piedmont Basin, at the northernmost offshoot of

the Mediterranean (cf. Dela Pierre *et al.*, 2011). This succession comprises an alternation of gypsum beds, dolomitic mudstones and diatomaceous layers (Fourtanier *et al.*, 1991), allowing a detailed reconstruction of the early diagenetic transformation of biogenic silica-rich and organic matter-rich sediments deposited in a restricted basin during a palaeoenvironmental crisis.

GEOLOGICAL AND STRATIGRAPHIC SETTING

Overview of Messinian salinity crisis events in the Mediterranean

Following the restriction of the connection with the Atlantic Ocean along the Rifian and Betic gateways, which started at approximately 7.2 Ma (Kouwenhoven & van der Zwaan, 2006), the Mediterranean turned into the youngest salt giant in Earth history during the MSC. Recent studies have highlighted that the MSC evolved through three main stages (e.g. Roveri *et al.*, 2014). During the first stage (5.97–5.60 Ma), sulphate evaporites referred to as the Primary Lower Gypsum unit (PLG) were deposited in the peripheral basins of the Mediterranean. The PLG unit consists of the rhythmic alternation of shales, mudstones and primary, *in situ* gypsum beds. The lithological cyclicity is interpreted to reflect precession-driven climate change, with shales and mudstones associated with humid climate at precession minima (insolation maxima) and gypsum coinciding with arid climate at precession maxima (insolation minima). Shales and mudstones are commonly characterized by high contents of dolomite and smectite, traditionally interpreted as reflecting a sabkha-like palaeoenvironment and the erosion of seasonally arid peri-Mediterranean palaeosoils, respectively (e.g. Chamley *et al.*, 1977; Friedman, 1973). During the second stage (5.60–5.55 Ma), the PLG unit was uplifted and eroded. The products of erosion were transferred downslope by various types of gravity flows (Manzi *et al.*, 2005), forming the Resedimented Lower Gypsum (RLG) unit, which consists of clastic gypsum deposits mixed with shales (Manzi *et al.*, 2021) that interfinger, at least in Sicily, with halite and potassium/magnesium salts. During the third stage

(5.55–5.33 Ma), a new evaporitic unit (Upper Gypsum) was deposited in the Southern and Eastern Mediterranean, whereas clastic sediments are found in the western and northern sectors of the basin. Both units are typified, in the upper part, by brackish water sediments associated with the so-called Lago Mare phase, whose origin is still being debated (e.g. Caruso *et al.*, 2020; Andreetto *et al.*, 2021; Carnevale & Schwarzahans, 2022).

Messinian salinity crisis record in the Piedmont Basin

The Piedmont Basin (**Fig. 1**) is a large wedge top basin filled with Eocene to upper Miocene sediments overlying a complex tectonic wedge of Alpine, Ligurian and Adria basement units juxtaposed during the meso-Alpine collisional event (e.g. Mosca *et al.*, 2010; Rossi & Craig, 2016; Rossi, 2017). The MSC sedimentary record consists of the PLG unit at the basin margins passing laterally into organic-rich and dolomite-rich shales towards the basin depocentre (e.g. Lozar *et al.*, 2018; Sabino *et al.*, 2021; Natalicchio *et al.*, 2021). The PLG unit consists of up to 15 lithological cycles made up of shale/mudstone and gypsum couplets (e.g. Natalicchio *et al.*, 2021). The sixth gypsum bed corresponds to a distinct marker bed (Sturani Key Bed; see Dela Pierre *et al.*, 2011), recording the appearance of two gypsum lithofacies not observed in the underlying beds that consist of vertically oriented selenite crystals: laminar gypsum (balatino, *sensu* Ogniben, 1957) and branching selenite, i.e. metre-sized flattened cones composed of horizontally oriented millimetre to centimetre-sized crystals (e.g. Natalicchio *et al.*, 2021). The lateral distribution of the gypsum lithofacies reflects the progressive deepening of the basin from south-west to north-east, whereas the vertical stacking pattern indicates basin shallowing. Interestingly, the non-evaporitic component of the PLG unit (i.e. the shale and mudstone interbeds that are the object of this study) is typified by high contents of dolomite, interpreted to be of microbial origin (e.g. Dela Pierre *et al.*, 2014). Isolated diatom moulds (Dela Pierre *et al.*, 2014) and thin layers of diatomaceous sediments have also been reported (Fourtanier *et al.*, 1991; Irace *et al.*, 2005), the latter exposed in the Bric

Cenciurio and Cascina Botto sections investigated in this study. The PLG unit is overlain by chaotic and clastic gypsum deposits of the Valle Versa Chaotic complex, corresponding to the local equivalent of the RLG unit, and by the Cassano Spinola Conglomerates, consisting of fluvial, lacustrine and marine sediments deposited during the third stage of the MSC (Dela Pierre *et al.*, 2011; Andreetto *et al.*, 2022).

MATERIAL AND METHODS

Sampling sites

Two sections exposing the PLG unit were studied (**Fig. 1**): the Bric Cenciurio section (44°45'45.0"N; 8°03'07.9"E) and the Cascina Botto section (44°44'59.6"N; 8°23'05.1"E). In both sections, gypsum layers are interbedded with dolomite-rich and diatomaceous sediments (Fourtanier *et al.*, 1991; Irace *et al.*, 2005). In the field, weathered surfaces on rocks were thoroughly removed and fourteen samples (thirteen from the Bric Cenciurio section and one from the Cascina Botto section, for the sake of comparison) were collected. Samples from the Bric Cenciurio section were wrapped in aluminium foil and stored at −20°C until further treatment.

Sedimentological and petrographic study

The lithology and sedimentological features of the non-evaporitic intervals of the PLG unit were documented. Fifteen petrographic, polished thin sections (thirteen perpendicular and two parallel to the bedding plane) were produced after epoxy impregnation of the samples from the Bric Cenciurio section (**Fig. 2**), and more than 100 chips of unconsolidated samples were studied using transmitted, reflected and UV light microscopy using a Leica DM 2770 P microscopy equipped with a digital photcamera (Leica Microsystems, Wetzlar, Germany). Scanning electron

microscopy (SEM) and energy dispersive X-ray spectroscopy (EDS) analyses were performed on thin sections (backscattered electron imaging, BSEI) and sediment chips (secondary electron imaging, SEI) after carbon coating, using a JSM IT300LV (Department of Earth Sciences of the University of Torino; JEOL Limited, Tokyo, Japan) and a Tescan S9000G, (Department of Chemistry of the University of Torino; Tescan, Brno, Czechia). For the diatom-bearing samples of the Bric Cenciurio section, only the dominant or more recurrent taxa observed on freshly broken subsamples are reported (for a comprehensive taxonomic list see Fourtanier *et al.*, 1991). Freshly-broken sediment chips from the Cascina Botto section were studied with SEM-EDS.

Elemental, mineralogical and dolomite C and O stable isotope analyses

Selected polished thin sections and freshly-broken sediment chips of a single sample of diatomaceous shales, a single sample of diatom-bearing mudstones and two samples of dolomitic mudstones from the Bric Cenciurio section (samples 10, 13, 3 and 2; see **Fig. 2**) have been semi-quantitatively analyzed by means of electron dispersive X-ray spectroscopy (EDS Oxford INCA Energy 200 equipped with INCA detector X-act SDD thin window; Oxford Instruments, Abingdon, UK), combining automated maps and manual check of single spots using the software AZtec® and INCA® (Oxford Instruments). The percentages of aluminium (Al), iron (Fe), potassium (K), magnesium (Mg) and Si obtained from 150 spots (50 for each analyzed lithology) were plotted on ternary diagrams following Konhauser & Urrutia (1999).

Bulk mineralogy of the same samples was characterized with X-ray powder diffraction (XRPD). Clay minerals *sensu lato* were characterized with the standard sequential characterization procedure (e.g. Brindley & Brown, 1961) on the silt-sized and clay-sized fraction (<20 µm) obtained by gravimetric separation. This fraction was saturated with Mg by continuous stirring overnight using a 1 M magnesium chloride (MgCl₂) solution. After Mg saturation, the excess MgCl₂ was removed by washing the sample in ultrapure water 18 MOhm and shaking it with an

elliptical shaker for two hours. The washing routine was repeated three times for each sample to avoid MgCl_2 precipitation during drying. The fraction was collected each time by centrifugation at 4000 RPM for 60 minutes. After the last rinse, the samples were deposited on glass slides and dried at room temperature to obtain oriented clay samples for further treatments. Swelling clay minerals were determined by vapour saturation of the oriented clay samples in glycol ethylene at 70°C for three hours. Thermally sensitive mineral phases were determined by heating the oriented clay samples at 300°C and 550°C for two hours, respectively. After each treatment, oriented clay samples were characterized with a Rigaku MiniFlex 600 benchtop X-ray diffractometer (Rigaku, Tokyo, Japan), Bragg-Brentano geometry, $\text{CuK}\alpha$ radiation, X-ray source operating at 40 kV and 15 mA; D/teX Ultra2 silicon strip detector; $2^\circ < 2\theta < 50^\circ$, step width 0.005° , scan speed $0.3^\circ/\text{min}$. XRPD patterns after each treatment were decomposed using the Fityk free curve fitting and data analysis software (Wojdyr, 2010) and analyzed to determine the clay minerals in the fine-grained fraction of each sample. Interlayered structures were simulated using the PyXRD free software (Dumon & Van Rast, 2016) to model X-ray diffraction patterns of disordered lamellar structures.

The bulk mineralogical characterization of the samples and quantitative analysis were performed using a Rigaku SmartLab XE X-ray diffractometer with Bragg-Brentano geometry, $\text{CuK}\alpha$ radiation, X-ray source operating at 40 kV, 30 mA; D/teX Ultra 250 HE silicon strip detector; $5^\circ < 2\theta < 80^\circ$, step width 0.01° , scan speed $1^\circ/\text{min}$. Data were analyzed using the Match! (Crystal Impact) phase analysis software. Quantitative analysis was performed using the Reference Intensity Ratio method with silicon as the internal reference standard.

Carbon ($\delta^{13}\text{C}$) and oxygen ($\delta^{18}\text{O}$) stable isotope analyses were conducted at the Department of Earth Sciences of the University of Milano (Italy) on six samples of dolomitic mudstones from the Bric Cenciurio section (samples 2, 3, 4, 5, 6 and 8; see **Fig. 2**). Analyses were performed using an automated carbonate preparation device (Gasbench II) and a Thermo Fisher Scientific Delta V Advantage continuous flow mass spectrometer (Thermo Fisher Scientific, Waltham, MA, USA). The powders of dolomitic samples were reacted with >99% orthophosphoric acid at 70°C for 8

hours. The carbon and oxygen isotope compositions are expressed in the conventional delta notation calibrated to the Vienna Pee-Dee Belemnite (V-PDB) scale by the international standards IAEA 603 and NBS-18. Most samples were analyzed twice and the average values are provided.

Analytical reproducibility for the analyses was better than $\pm 0.1\%$ for both $\delta^{13}\text{C}$ and $\delta^{18}\text{O}$ values. Corrections for different reaction times and fractionation for dolomite were carried out using the protocol of Kim *et al.* (2015).

Total organic carbon and biomarkers

Total organic carbon (TOC) quantification and lipid biomarker analyses were performed at the Institute for Geology of the University of Hamburg (Germany) on two samples of diatomaceous shales, one sample of diatom-bearing mudstones and three samples of dolomitic mudstones from the Bric Cenciurio section (samples 10, 12, 13, 8, 3 and 2; see **Fig. 2**). For carbon content analyses, the samples were powdered and split in two aliquots. The first aliquot was heated to 1350°C to measure the total carbon (TC) content using a LECO SC-144DR Carbon Analyzer equipped with an infrared detector (Leco Corporation, St. Joseph, MI, USA). The second aliquot was first heated to 550°C for 5 hours to remove the TOC and subsequently heated to 1350°C to measure total inorganic carbon (TIC). The TOC content was then calculated using the formula $\text{TOC} = \text{TC} - \text{TIC}$. Prior to the measurements, a standard (Synthetic Carbon Leco 501-034; 1.01 ± 0.02 carbon%) was analyzed for reference.

For lipid biomarker analyses, aliquots of the six samples above were dried overnight in an oven (45°C) and subsequently cleaned by removing a few millimetres of sediment from the external surfaces with a chisel. A homogenous powder was then produced for each sample using mortar and pestle. The samples were saponified with 6% potassium hydroxide in methanol (2 h, 80°C) and subsequently extracted manually via repeated ultrasonication, using a mixture of dichloromethane (DCM) and methanol (3:1), until the extracts became colourless. The combined extracts were

cleaned by washing with MilliQ water, and carboxylic acid salts in the aqueous phase were transferred to the organic phase by adding 10% hydrochloric acid (HCl) until the pH was approximately 2. After extraction, the previously extracted powder of the three dolomite-rich samples was decalcified with 10% HCl according to the procedure described by Birgel *et al.* (2014) and subsequently saponified and extracted a second time according to the procedure described above; the second extract tends to yield the molecular signature preserved within the carbonate mineral matrix. The total lipid extracts obtained after the two extractions (before and after decalcification) were separated into maltene (*n*-hexane-soluble) and asphaltene (DCM-soluble) fractions (see Natalicchio *et al.*, 2019, for further details). Maltene fractions were further separated into four different fractions of increasing polarity using aminopropyl-bonded silica gel column chromatography (Supelco glass cartridge: 6 ml, 500 mg, DSC-NH2) and a sequence of organic solvents: (i) hydrocarbons using *n*-hexane; (ii) ketones using *n*-hexane:DCM (3:1); (iii) alcohols using DCM:acetone (9:1); and (iv) carboxylic acids using 2% formic acid in DCM:formic acid. Compounds in the alcohol fraction were derivatized by adding a mixture of pyridine and (N,O)-bis(trimethylsilyl)trifluoroacetamide (BSTFA) to measure the alcohols as their TMS-derivatives. For hydrocarbons, alcohols and carboxylic acids, internal standards were added prior to extraction (5 α -cholestane, 1-nonadecanol, 2-me-C₁₈ fatty acid, and the dialkyl glycerol diether *n*-C₁₈/*n*-C₁₈). Compounds were identified using a gas chromatography–mass spectrometer (GC–MS) system, a Thermo Scientific Trace GC Ultra coupled to a Thermo Scientific DSQ II mass spectrometer. Compound assignment was based on relative retention times and published mass spectral data. In this study, a detailed quantification of lipids is only provided for the alcohol fraction, which revealed a high abundance and a good preservation of compounds produced by algae, bacteria and archaea (see below).

RESULTS

Field observations

The Bric Cenciurio section consists of an alternation of decimetre to metre-thick dolomitic mudstone and gypsum beds, the latter displaying different lithofacies (**Fig. 2**). The first two layers consist of clastic gypsum (gypsum-rudites grading into gypsum-arenites), whereas the overlying beds are made up of primary gypsum. In particular, the third bed contains decimetre-sized bottom-grown twinned selenite crystals, forming metre-sized cones in the upper part, separated by dolomitic mudstones (**Fig. 2**). The third gypsum bed, *ca* 3 m-thick, records the appearance of the branching selenite lithofacies and corresponds to the so-called Sturani Key Bed (**Fig. 2**; see Natalicchio *et al.*, 2021, for details). The Sturani Key Bed allows physical correlation with other Messinian sections of the Piedmont Basin (Dela Pierre *et al.*, 2011). Branching selenite is observed also in the upper two beds, *ca* 2 and 1 m thick, respectively. Above the Sturani Key Bed, a *ca* 20 cm-thick, whitish to pale brown diatomaceous shale layer is observed below a decimetre-thick slumped bed. In the upper part of the section, a prominent carbonate bed is found, containing diagenetic gypsum nodules and cavities derived from the dissolution of gypsum crystals. Above, a whitish to pale brown diatomaceous shale layer, *ca* 50 cm thick, underlies a decimetre-thick slumped layer. A *ca* 20 cm thick, faintly pinkish diatom-bearing mudstone layer is situated below the fourth gypsum bed (**Fig. 2**).

The Cascina Botto section starts with the alternation of homogeneous marls and laminated mudstones belonging to the Sant'Agata Fossili Marls (upper Tortonian–lower Messinian). The lower boundary of the PLG unit was traced at the base of sandy and clayey beds interrupted by diagenetic carbonate masses and dolomitic mudstones; a decimetre-thick diatomaceous layer was also recognized (Irace *et al.*, 2005, for details).

Sedimentology and petrography

Three lithofacies can be distinguished in the non-evaporitic interbeds of the PLG unit exposed in the Bric Cenciurio and Cascina Botto sections on the basis of the content and preservation of biogenic silica: (i) diatomaceous shales, typified by very high contents of pristine diatom valves; (ii) diatom-bearing mudstones, with common and poorly-preserved biosiliceous remains; and (iii) dolomitic mudstones, typified by traces of biogenic silica represented by close to completely dissolved diatom valves and etched sponge spicules.

Diatomaceous shales

The diatomaceous shales are characterized by fine lamination generated by the alternation of submillimetre-thick, white and dark (greyish, reddish to pale-brown) laminae (**Fig. 3A and B**).

Clear laminae enclose only minor clay-sized and silt-sized grains within an opal matrix (**Fig. 3C**).

Locally, gypsum rosettes displace single laminae or bundles of laminae (**Fig. 3D**). Contacts between laminae are sharp and most of the opal-rich laminae are laterally continuous (**Fig. 3E and F**); the latter are composed of closely stacked diatom valves and subordinate lensoidal pockets of clay-sized and silt-sized grains (**Fig. 3G**). In contrast, the laminae appearing dark in reflected light have a higher clay-sized and silt-sized grain content (**Fig. 3C**), with diatom valves and sponge spicules as accessory components (**Fig. 3H**). Dolomite and pyrite framboids are rare.

Opal-rich laminae are formed by dense mats of marine planktonic diatoms, notably well preserved specimens of Thalassionemataceae (*Thalassionema* spp. and *Thalassiothrix longissima*; **Fig. 4A and B**) and fragmented remains of Rhizosoleniaceae (**Fig. 4C and D**). Scattered specimens of other planktonic (for example, *Asterolampra* spp., *Bacteriastrum* sp., *Coscinodiscus* spp., *Chaetoceros* resting spores, *Nitzschia* spp., *Thalassiosira* spp.) and benthic (for example, *Cymatosira* spp.) diatoms, as well as chrysophyte cysts and silicoflagellates (*Stephanocha speculum*, commonly represented by aberrant specimens) occur in both opal-rich and clayey-silty laminae.

Diatom-bearing mudstones

The diatom-bearing mudstones are characterized by the alternation of submillimetre-thick, pale and brownish-reddish laminae, irregularly enriched in lensoidal, rhombohedral or roundish silt-sized gypsum grains and locally interrupted by greyish, massive layers (**Fig. 5A**). Close observation reveals compositional contrast between individual laminae, caused by minor fluctuation in the content of silt-sized grains (**Fig. 5B to D**). The brownish-reddish laminae contain abundant pyrite framboids and unidentified micron-sized grains, possibly corresponding to framboid microcrystallites (**Fig. 5B and E to G**); the laminae have high Fe and Si contents. The diatom assemblage comprises both planktonic marine (*Actinocyclus* cf. *octonarius* var. *tenellus*; Thalassionemataceae; **Fig. 5H to J**) and benthic, marine to brackish taxa (biddulphoids, naviculoids, *Surirella* spp.; **Fig. 5K to M**). The diatom remains are affected by dissolution, and are commonly coated with flocky lumps of clay minerals (**Fig. 5I to L**). Locally, thin threads occur at the interface between diatom valves and surrounding clays (**Fig. 5N**). Sponge spicules are better preserved than diatom valves, but also show etching pits (**Fig. 5O**).

Dolomitic mudstones

Dolomitic mudstones are characterized by closely to widely-spaced lamination defined by submillimetre to millimetre-thick, whitish to pale brown and reddish laminae (**Fig. 6A to C**); packets of laminae are locally disrupted by brownish to greyish millimetre to centimetre-thick massive to graded layers (**Fig. 6B**). Reddish laminae contain abundant pyrite framboids similar to the reddish diatom-bearing mudstones. Silt-sized terrigenous grains (quartz, feldspars and micas) are common and often surrounded by a reddish halo and pyrite framboids; the edges of terrigenous grains are commonly corroded (**Fig. 6D and E**). Blackish, lensoidal amorphous aggregates (**Fig.**

6F) and partially corroded gypsum crystals are present (Fig. 6F to H). All components are embedded in a finely crystalline matrix composed of spheroidal dolomite microcrystals, some of which exhibit a hollow core, and clay minerals. Dolomite microcrystals are a few microns in diameter and show a globular to cauliflower-like morphology (Fig. 7A to D). Locally, aggregations of framboids occur (Fig. 7E and F). Poorly preserved sponge spicules (Fig. 8A to D) and benthic diatom remains (Fig. 8E and F) are rare.

Elemental composition, mineralogy and dolomite C and O stable isotopes

The diatomaceous shales are typified by high Si contents caused by diatom valves (Fig. 9A); some spots of this lithology are characterized by high Al and Fe contents (Fig. 9B). Elements other than Si are mostly present in the laminae enriched in silt-sized and clay-sized terrigenous grains (Fig. 9C). In contrast, altered diatom remains are enriched in Al, Fe, K and Mg in the diatom-bearing mudstones (Fig. 9D and E). Interestingly, the elemental composition of these remains is similar to the composition of the finely crystalline clay minerals associated with spheroidal dolomite of the dolomitic mudstones (Fig. 9F and G). A trend of progressive enrichment in Fe, K and Mg from the pristine biosiliceous remains in diatomaceous shales over altered biosiliceous remains in the diatom-bearing mudstones to clay minerals in dolomitic mudstones is nicely illustrated by ternary diagrams (Fig. 10).

According to XRPD analysis (see **Supporting Information**), dolomite content varies from 61% in the dolomitic mudstones to 9.7% in the diatom-bearing mudstones and 1.8% in the diatomaceous shales (Table 1). The poorly crystalline clay fraction of all lithologies can mostly be attributed to illite–smectite (I-S) interlayers and vermiculite. An associated, more crystalline fraction, most likely of detrital origin, is composed of chlorite, plagioclase and quartz (Fig. 11). In the dolomitic mudstones, at least two families of interlayered structures with swelling properties have been recognized in the poorly crystalline fraction: a smectite–smectite (SS) interlayer,

represented by a double population with slightly different values of d_{001} and same 0 (random) *reichweite ordering*, and illite–chlorite–smectite (ICS) mixed-layers with higher ordering (*reichweite ordering 2*). The poorly crystalline fractions of the diatom-bearing mudstones and the diatomaceous shales show similar composition.

The $\delta^{13}\text{C}$ and $\delta^{18}\text{O}$ values of the samples of dolomitic mudstones range from -5.4 to -0.6% and from $+3.4$ to $+6.8\%$, respectively (**Table 2**).

Total organic carbon and biomarkers

The TOC contents of the studied lithologies range from 0.3 to 2.3% (**Table 3**). The dolomitic mudstones (samples 2, 3 and 8) show rather constant TOC contents, 2% on average, whereas the diatomaceous deposits are characterized by lower TOC contents, ranging from 0.3% (diatom-bearing mudstones, sample 13) to 0.7% (diatomaceous shales, sample 10).

Lipid biomarkers of the alcohol fraction are generally well preserved (**Fig. 12**; see **Supporting Information**), although overall contents vary from high in the diatomaceous shales (up to 530 $\mu\text{g/g}$ TOC in sample 10), over intermediate in the diatom-bearing mudstones (average *ca* 281 $\mu\text{g/g}$ TOC in sample 13), to low in the dolomitic mudstones (samples 2, 3, 8; *ca* 14 $\mu\text{g/g}$ TOC on average; **Fig. 12A**, **Table 3**; see **Supporting Information**).

An even-over-odd carbon number predominance of *n*-alcohols (ranging from *n*-C₁₆ to *n*-C₃₄) is present in the studied lithologies with the highest contents in the diatomaceous shales (up to *ca* 180 $\mu\text{g/g}$ TOC) and diatom-bearing mudstones (*ca* 166 $\mu\text{g/g}$ TOC), while the dolomitic mudstones revealed lower contents (up to *ca* 14 $\mu\text{g/g}$ TOC; **Table 3**). Long-chain *n*-alcohols from *n*-C₂₆ to *n*-C₃₂, sourced from plant waxes (e.g. Rommerskirchen *et al.*, 2006; Hemingway *et al.*, 2016), are abundant in all samples and the dominant compounds in the diatom-bearing mudstones and dolomitic mudstones (**Table 3**; **Fig. 12A**).

Phytoplankton-derived lipid biomarkers are prominent in the diatomaceous shales. Among them, long-chain 1,X diols (C₂₆–C₃₂) are very abundant, corresponding to up to 67% of all alcohols (**Fig. 12A and B**). In particular, the 1,X-C₂₈₋₃₀ diol homologues account for 24 (sample 12) to 54% (sample 10) of all alcohols for the diatomaceous shales and represent 26% in case of the diatom-bearing mudstones (see **Supporting Information**). The X indicates the position of a hydroxyl group either at carbon 12, 13, 14 or 15. Among them, 1,14-C₂₈ and 1,14-C₃₀ diols are the most abundant, comprising up to 85% of 1,X-C₂₈ diols and between 91 to 97% of 1,X-C₃₀ diols, respectively (see **Supporting information**). Minor keto-ols comprising C₃₀₋₃₄ carbons are present in the diatomaceous shales, accounting for less than 9% of all alcohols. Keto-ols probably derive from the oxidation of the corresponding diols (e.g. Versteegh *et al.*, 1997; Ferreira *et al.*, 2001), agreeing with a phytoplankton source. Several phytoplankton-derived sterols are also present in the diatomaceous shales, including high amounts of brassicasterol (up to 19 µg/g TOC in sample 10) and 24-methylenecholesterol (up to 5 µg/g TOC in sample 12), common biomarkers of various diatoms (cf. Rampen *et al.*, 2010) and dinosterol (up to 11 µg/g TOC in sample 12), typically sourced by dinoflagellates and diatoms (Volkman *et al.*, 1993). β-sitosterol and its degradation product stigmastanol are also abundant, representing 3 to 4% of all alcohols in diatomaceous shales and diatom-bearing mudstones. These compounds are chiefly produced by eustigmatophytes, land plants and in minor amount by diatoms (cf. Rampen *et al.*, 2010). However, their strict association with pristine diatom valves suggests that they were mostly sourced by diatoms. Short-chain *n*-alcohols *n*-C₁₆ to *n*-C₂₅ also contribute to the pool of probable phytoplankton-derived lipids, but represent less than 4% of all lipids in the alcohol fraction (**Table 3, Fig. 12A**).

A different relative proportion between the algal-sourced lipids, sterols, diols and keto-ols is observed for the dolomitic mudstones (**Fig. 12B**). In this lithology, C₂₈₋₃₂ diols exhibit significantly lower contents (less than 1.1 µg/g TOC) in samples 2 and 3, and are absent in sample 8, whereas the algal derived C₂₄₋₃₆ keto-ols predominate with contents as high as 2.7 µg/g TOC, representing up to 33% of total alcohols in sample 8 (**Table 3**). Contents of algal sterols are also lower than in the

diatomaceous shales and diatom-bearing mudstones (<7% of the total alcohols), with stigmastanol, dinosterol and dinostanol predominating. Similarly, contents of the short-chain *n*-alcohols *n*-C₁₆ to *n*-C₂₆ are also lower (as high as 3.8 µg/g TOC in sample 3), yet their relative proportion is higher than in the diatomaceous shales and diatom-bearing mudstones, making up to the 20% of the measured alcohols (Fig. 12A).

The decalcification procedure applied for the dolomitic mudstones (see *Material and methods* section) released an additional lipid assemblage (Fig. 12C; see **Supporting Information**). For sample 8, the majority of lipid biomarkers was only released after the second extraction following decalcification (see **Supporting Information** for details). In particular, C₂₀₋₂₀ archaeol, phytanol and *sn*2-, *sn*3-phytanylglycerol monoethers (ph-monoethers), which are common lipids of archaea (e.g. De Rosa & Gambacorta, 1988; Hoffmann-Sell *et al.*, 2011; Birgel *et al.*, 2014), were found in all samples with highest contents in sample 8. Accessory C₁₆ monoalkyl glycerol monoether (MAGE *n*-C_{16:0}), a biomarker of various bacteria including sulphate-reducing bacteria (Grossi *et al.*, 2015), was detected in samples 2 and 3. This major MAGE, already apparent in the total ion current, is accompanied by other MAGEs ranging from 14 to 20 carbons; the latter compounds were recognized when scanning for the diagnostic *m/z* 205 on the GC-MS, and include terminally-branched MAGEs with 15 to 17 carbons (see Fig. 12C). The pentacyclic triterpenoid tetrahymanol (Sinninghe Damsté *et al.*, 1995; Natalicchio *et al.*, 2017) was also only detected in the extracts after decalcification.

DISCUSSION

Evidence of primary productivity by diatoms during the Messinian salinity crisis

Petrographic and organic geochemical data (Table 4) suggest that marine productivity dominated by planktonic diatoms, generating organic matter and biogenic silica, persisted during

the early stage of the MSC (cf. Fourtanier *et al.*, 1991; Pellegrino *et al.*, 2021). The well-preserved diatom valves in the diatomaceous shales (**Fig. 4**) and the altered remains of diatoms in the diatom-bearing mudstones (**Fig. 5I to N**) represent the most obvious evidence of high biosiliceous productivity in a marine environment. The high abundance of rhizosolenioid diatoms and Thalassionemataceae in the diatomaceous shales of the Bric Cenciurio section (**Fig. 4**) is in line with a scenario typified by the intermittent alternation of water column stratification (associated with surface oligotrophy) and water column mixing (associated with surface eutrophic conditions). Stratified waters during warm periods may have favoured the build-up of rhizosolenioid-dominated mats at the nutricline-thermocline and a deep chlorophyll maximum (e.g. Kemp *et al.*, 2000). Subsequent vertical mixing during cool and dry periods destabilized the mats, promoting their fast deposition ('fall dump') on the seafloor (cf. Kemp *et al.*, 2000). In contrast, the Thalassionemataceae probably thrived in the upper layer of the water column, following a nutrient pulse provided by riverine input in accord with the scattered occurrence of reworked chrysophycean cysts and benthic diatoms (cf. Pellegrino *et al.*, 2020a) or water column mixing, forming large aggregates. Once nutrients were exhausted, diatom aggregates rapidly sank toward the seafloor. High terrestrial input is evident from the high content of long-chain *n*-alcohols (e.g. Natalicchio *et al.*, 2019; **Fig. 12A**). Elevated biosiliceous productivity is also reflected by the high content of algal-derived lipid biomarkers in the diatomaceous shales (**Fig. 12B and C**), including the 1,14-C₂₈₋₃₀ diols and the C₂₇₋₂₉ sterols (i.e. brassicasterol, β -sitosterol, 24-methylenecholesterol) (Volkman *et al.*, 1999; Rampen *et al.*, 2010, 2022). In particular, C₂₈ and C₃₀ 1,14 diols are common constituents of modern rhizosolenioid diatoms (i.e. *Proboscia*; Sinninghe Damsté *et al.*, 2003; Rampen *et al.*, 2022), whereas 24-methylenecholesterol has been found as the most common sterol in the Thalassiosirales, *Coscinodiscus* sp. and *Chaetoceros* sp. (Volkman & Hallegraeff, 1988; Rampen *et al.*, 2010). The molecular fossil inventory is therefore consistent with the microfossil content.

In contrast, the close to total absence of biosiliceous remains in the dolomitic mudstones would suggest that biosiliceous productivity was temporarily interrupted. Nevertheless, the

occurrence of etched sponge spicules and altered benthic diatom remains in these sediments (**Fig. 8**) suggest that this was not the case. These features, along with the presence of corroded siliciclastic grains (**Fig. 6D and E**), point to a severe alteration of both biogenic and lithogenic silica pools. The absence of planktonic diatom remains in these sediments probably reflects their higher susceptibility to dissolution. Actually, planktonic diatoms are on average less silicified than benthic diatoms (e.g. Conley *et al.*, 1990). Furthermore, phytoplankton-derived lipids archived in dolomitic mudstones (**Fig. 12**) are a compelling evidence of persistent biosiliceous productivity. The lipid biomarker inventory of dolomitic mudstones includes dinosterol and dinostanol and accessory 1,X-C₂₈₋₃₀ diols, representing the most abundant phytoplankton-derived lipids found in the diatomaceous shales. In the absence of microfossil remains supporting the diatomaceous origin of the diols, other sources of these compounds cannot be excluded, including eustigmatophyte microalgae (e.g. Volkman *et al.*, 1999; Rampen *et al.*, 2022). However, keto-ols are typically considered as degradation product of diols (e.g. Versteegh *et al.*, 1997; Ferreira *et al.*, 2001). Therefore, the near to complete absence of siliceous microfossils and the dominance of long-chain keto-ols in the dolomitic mudstones over long-chain diols probably reflects bottom water or surface sediment conditions unfavourable for the preservation of biogenic silica.

Bottom water conditions

Petrographic, mineralogical and geochemical evidence (**Figs 6 and 7; Tables 1 and 2**) suggests that the dolomitic mudstones formed in an anoxic environment possibly below a stratified water column (cf. Sabino *et al.*, 2021). First, the TOC content is high (from 2.04 to 2.32%; see **Table 3**), which agrees with oxygen-depleted bottom water conditions, favouring the preservation of organic carbon. Second, the sediments are composed of dolomite (>47%; see also **Table 1**). Dolomite is a common component of the Messinian sedimentary successions of the Mediterranean (e.g. Kelts & McKenzie, 1984; Bellanca *et al.*, 1986; Pierre *et al.*, 2002), and its origin had first

Accepted Article

been related to hypersaline conditions in very shallow, sabkha-like environments (e.g. Friedman, 1973; Di Bella *et al.*, 2020), chiefly explained by positive $\delta^{18}\text{O}$ values indicative of evaporated seawater. However, dolomite also commonly forms in organic-rich, strongly reducing and sulphidic sediments after pronounced bacterial sulphate reduction (e.g. Kelts and McKenzie, 1984; de Lange & Krijgsman, 2010; Dela Pierre *et al.*, 2012; Lu *et al.*, 2018; Natalicchio *et al.*, 2021; Sabino *et al.*, 2021). Bacterial sulphate reduction tends to increase alkalinity, favouring the precipitation of ^{13}C -depleted carbonate minerals including dolomite (e.g. Vasconcelos *et al.*, 1995; Sanz-Montero *et al.*, 2009; Bontognali *et al.*, 2010). At high sulphide levels, the kinetic inhibition of dolomite formation under surface conditions is overcome, and dolomite forms by sulphide catalysis and subsequent ordering during early diagenesis (Zhang *et al.*, 2012; Lu *et al.*, 2021). The hydrogen sulphide released by bacterial sulphate reduction also reacts with iron to form pyrite, a mineral common in the studied lithologies (e.g. Berner, 1984). Since sulphate-reducing bacteria are mostly obligate anaerobes (e.g. Londry & Des Marais, 2003; Dolla *et al.*, 2006), the presence of microbially-formed dolomite is an indicator of anoxic conditions in pore waters (e.g. Petrash *et al.*, 2017; Li *et al.*, 2021). In the studied samples, the spheroidal and cauliflower-like morphology of the dolomite crystals, the hollow core and negative $\delta^{13}\text{C}$ values (from -5.4 to -0.6% ; see **Table 2**) agree with a microbial origin (cf. Vasconcelos *et al.*, 1995; Bontognali *et al.*, 2010; Lindtke *et al.*, 2011). The absence of evidence of compaction suggests that dolomite was formed in porous sediments at shallow depth below the sediment–water interface. A bacterially-induced formation of dolomite is corroborated by the characteristic MAGE patterns and, particularly, the circumstance that MAGEs are only released after decalcification of the dolomite crystal lattice. The obtained MAGE patterns resemble compound inventories of sulphate-reducing bacteria from cultures, sediments and authigenic minerals (cf. Hinrichs *et al.*, 2000; Rütters *et al.*, 2001; Heindel *et al.*, 2012; Guido *et al.*, 2013; Grossi *et al.*, 2015; Vinçon-Laugier *et al.*, 2016). These biomarkers of sulphate-reducing bacteria, in accord with low $\delta^{13}\text{C}_{\text{dolomite}}$ values, therefore suggest a tight connection between metabolism (i.e. sulphate reduction) and dolomite formation.

Tetrahymanol is commonly considered as an indicator of water column stratification (e.g. Sinninghe Damsté *et al.*, 1995; Natalicchio *et al.*, 2017). However, since tetrahymanol was only detected in extracts after decalcification, a benthic source organism is more likely. Tetrahymanol is produced by many organisms (anoxygenic phototrophs, ciliates, aerobic methanotrophic bacteria and many others), but the majority of the known producers thrive in the water column. Two possible benthic source organisms are aerobic methanotrophic bacteria (e.g. Cordova-Gonzalez *et al.*, 2020, and references therein), and sediment-thriving, heterotrophic ciliates (Werne *et al.*, 2002, and references therein). The absence of other lipids of methanotrophic bacteria and of evidence of methane oxidation makes these bacteria an unlikely source. Therefore, benthic ciliates are the most likely producers of tetrahymanol. Interestingly, marine ciliates preferably live in porous, loose, organic-rich sediments, and can tolerate anoxic conditions (Werne *et al.*, 2002).

Unlike for the dolomitic mudstones, dolomite and pyrite framboids are very scarce in diatomaceous shales. Similarly, lipids of sulphate-reducing bacteria have not been detected in diatomaceous shales, suggesting that bacterial sulphate reduction was apparently less pronounced, probably suppressed by temporary oxygenated conditions at the seafloor and in the upper part of the sedimentary column. The diatom assemblages in the studied samples point to the intermittent mixing of the water column favouring bottom water oxygenation (e.g. Alfken *et al.*, 2021; see above). Similarly, low TOC contents of the diatomaceous shales in spite of high biosiliceous productivity agree with the notion that organic matter was mostly degraded aerobically, as hypothesized for other Neogene Mediterranean (e.g. Pérez-Folgado *et al.*, 2003; Pellegrino *et al.*, 2020a,b) and global (e.g. White *et al.*, 1992; Koizumi & Yamamoto, 2018) diatomaceous deposits. Such a scenario is in contrast with the laminated fabric of diatomaceous shales (**Fig. 3E and F**), which suggests the absence of bioturbation, and with the well-preserved algal lipids suggesting limited biodegradation. However, lamination cannot be considered *per se* as evidence for anoxic conditions since rapid deposition of diatom mats, such as those observed in the studied diatomaceous shales, may produce laminated sediments even under oxygenated bottom water

conditions. It has been shown that tensile-strength deriving from the close entanglement of diatom valves (**Fig. 4**) is able to inhibit benthic bioturbation (Kemp & Baldauf, 1993; Bodén & Backmann, 1996; Pike & Kemp, 1999; Shimada *et al.*, 2008; Pellegrino *et al.*, 2020b).

Lamination of diatomaceous shales is only deformed by syngenetic growth of gypsum rosettes. The absence of palaeontological evidence of shallow and hypersaline depositional conditions (i.e. presence of halophilic benthic diatoms and lipids of halophilic archaea) suggests that gypsum was not formed by evaporation. In fact, similar features have been observed in open ocean organic-rich and methane-rich sediments, where gypsum forms from the oxidation of dissolved sulphide and sulphide minerals resulting from bacterial sulphate reduction (e.g. Muza & Sherwood, 1983; Lin *et al.*, 2016). Therefore, it is suggested that the Castagnito gypsum rosettes are the product of sulphide oxidation, even though additional geochemical data will be needed to confirm this hypothesis.

Fate of biogenic silica and organic matter

Dolomitic mudstones record persistent water column stratification and bottom water anoxia (cf. Sabino *et al.*, 2021). In this lithology, biogenic silica is scattered and poorly preserved. Such a feature is surprising since biogenic silica preservation is supposed to be favoured by oxygen depletion (e.g. Sturani & Sampò, 1973; Birnbaum & Wireman, 1985; Hüsing *et al.*, 2009; Zachariasse *et al.*, 2021) because of: (i) limited bioturbation reworking biogenic silica; (ii) the assumed inefficiency of anaerobic bacteria to consume the organic layer protecting diatom frustules from dissolution; and (iii) supposed establishment of acidic conditions favouring silica preservation; silica preferentially dissolves at higher pH (e.g. Ehrlich *et al.*, 2010; Smrzka *et al.*, 2015). However, growing evidence from both modern and ancient sedimentary environments suggests that organic-rich and oxygen-poor conditions can be detrimental for the preservation of biogenic silica and even

lithogenic silica, casting doubt on the general attribution of diatomaceous deposits to the establishment of anoxia (e.g. Hiebert & Bennett, 1992; Spagnoli & Bergamini, 1997; Souchu *et al.*, 1998; Belias *et al.*, 2007; Villnäss *et al.*, 2012; Abe *et al.*, 2014; Ekeröth *et al.*, 2016; Lehtimäki *et al.*, 2016; Siipola *et al.*, 2016; Huggett *et al.*, 2017; Petranich *et al.*, 2018; Dale *et al.*, 2020). In particular, under anoxic conditions, bacterially-mediated anaerobic degradation of organic matter plays a critical role in modulating the pH of pore waters, a fundamental parameter for biogenic silica preservation (e.g. Ehrlich *et al.*, 2010). For example, dissimilatory iron reduction – a proton-consuming process (e.g. Howell *et al.*, 1998) – and bacterial sulphate reduction – though depending on the electron donors involved (for example, formate, hydrogen) – promote the rise of pore water pH (e.g. Mazzullo 2000, Gallagher *et al.*, 2012, 2014; Han *et al.*, 2016), favouring silica dissolution (e.g. White *et al.*, 1992; Jurkowska *et al.*, 2019; Neumeister *et al.*, 2020).

Besides dolomite and a clay-sized and silt-sized terrigenous chlorite, plagioclase and quartz (**Figs 6D, 6E and 11**), dolomitic mudstones are typified by poorly crystalline clay minerals mostly consisting of I-S interlayers (**Figs 7A to D and 11**). The fact that their composition overlaps with the composition of the clay coating diatom remains found in the diatom-bearing mudstone, and in rare cases also in the dolomitic mudstones (**Fig. 10**), suggests that these poorly crystalline clays derive from an original biosiliceous source and are authigenic. In addition, the close association of clays and dolomite microcrystals (**Fig. 7A to D**) indicates that authigenic clay formation was penecontemporaneous with the precipitation of microbial dolomite. Interestingly, the clay minerals interpreted as authigenic display a flaky habit, which suggest that they precipitated onto a former organic template such as extracellular polymeric substances (EPS) produced both by bacteria and diatoms (cf. Bhaskar & Bhosle, 2005). Actually, the threads closely associated with diatom remains (**Fig. 5N**) could represent mineralized EPS structures.

Neoformation of clay minerals requires availability of alkalinity (HCO_3^-), free cations (Al^{3+} , Fe^{2+} , K^+ , Mg^{2+}) and dissolved silica (Michalopoulos & Aller, 1995; Rahman, 2019). Such conditions were probably favoured by anaerobic bacterial communities, and in particular by

Accepted Article

sulphate reducers thriving on the organic matter mostly provided by siliceous primary producers. Bacterial sulphate reduction therefore probably triggered concomitant precipitation of authigenic dolomite and dissolution of biogenic silica through an increase of pore water pH (**Fig. 13A**). In the case of the studied Piedmont Basin lithologies, biogenic silica dissolution and consequent release of dissolved silica are illustrated by: (i) rare, yet corroded remains of sponge spicules, which are more silicified and therefore more resistant to dissolution than diatom frustules; and (ii) partially dissolved diatom remains in the dolomitic mudstones from the Bric Cenciurio and Cascina Botto sections (**Fig. 8**). Such close to complete absence of biogenic silica is in line with the greater susceptibility to dissolution of amorphous biogenic silica compared to crystalline lithogenic silica (Ehrlich *et al.*, 2010). However, the reddish halo around corroded margins of silt-sized grains (**Fig. 6D and E**) is taken as evidence of the alteration of lithogenic material (cf. Sanz-Montero *et al.*, 2009). This process apparently provided an additional source of dissolved silica and pore water cations (**Fig. 13A**), enhancing clay neoformation. A biotic contribution to the corrosion of lithogenic material is possible since bacterial biofilms may attach to the surface of silicate grains for scavenging nutrients (e.g. Hiebert & Bennet, 1992; Ullman *et al.*, 1996).

Interestingly, neoformed clays consists of I-S interlayers (**Fig. 11**), which are intermediate products of the transformation of smectite into illite. Such progressive transformation is considered a late diagenetic, abiotic process affecting smectite-rich sediments (e.g. Pollastro, 1990; Compton, 1991; Wilson *et al.*, 2016). The progressive ordering (from *reichweite* 0 to 3) of the I-S interlayers, reflects the percentage of illite, which is correlated to burial depth and thermal gradient (e.g. Wilson *et al.*, 2016). However, recent studies have highlighted the role of microbial communities in catalyzing smectite to illite transformation, resulting in a very fast conversion at ambient conditions in the order of weeks (e.g. Kim *et al.*, 2004, 2019; Liu *et al.*, 2012). In organic-rich sediments, iron-reducing and sulphate-reducing bacteria can promote illitization of smectite, coupling organic matter oxidation and metal, notably iron, reduction (e.g. Kim *et al.*, 2004, 2019; Liu *et al.*, 2012). In case of the Piedmont Basin, geological reconstructions (e.g. Dela Pierre *et al.*, 1995) and

petrographic and sedimentological observations (for example, absence of significant compaction and anhydrite after gypsum, Dela Pierre *et al.*, 2011) rule out burial diagenesis as a trigger of the conversion of smectite to illite. Therefore, it is suggested that this process was mediated by bacteria, in particular sulphate reducing bacteria (cf. Liu *et al.*, 2012). Interestingly, smectite to illite transformation tends to alter the oxygen isotopic composition of pore waters. Smectite-dominated clay progressively loses its interlayer water that is enriched in ^{18}O (e.g. Dählmann & de Lange, 2003). Carbonate minerals precipitating from such fluid will consequently show positive $\delta^{18}\text{O}$ values (e.g. Dählmann & de Lange, 2003). Interestingly, many Messinian dolomite-rich beds of the Mediterranean, including those studied here, show positive $\delta^{18}\text{O}$ values, which has been interpreted to reflect evaporated seawater and hypersaline conditions (e.g. McKenzie *et al.*, 1979; Bellanca *et al.*, 2001; Caruso *et al.*, 2015; Tzevahirtzian *et al.*, 2022). Alternatively, some of the ^{18}O enrichment may result from smectite-to-illite transformation, rather than seawater evaporation.

In contrast to dolomitic mudstones, the Piedmont Basin diatomaceous shales formed when the water column was intermittently mixed and stratified and bottom waters were more oxygenated, favouring the excellent preservation of biogenic silica. More molecular oxygen leads to more aerobic remineralization of organic matter and more carbon dioxide produced, lowering pore water pH (e.g. Silburn *et al.*, 2017), thereby inhibiting biogenic silica dissolution (**Fig. 13B**). The diatomaceous mudstones represent an intermediate lithology between dolomitic mudstones and diatomaceous shales. While their dolomite content is lower than that of dolomitic mudstones (9.7% versus 46.9–61.1%, respectively; see **Table 1**), diatomaceous mudstones commonly contain altered diatom remains coated by authigenic clay. In this case, siliceous microfossils were only partially dissolved, probably because of a low rate of bacterial sulphate reduction (low dolomite contents and absence of molecular fossils of sulphate-reducing bacteria) resulting from redox conditions intermediate between those prevailing during dolomitic mudstone (oxygen-depleted) and diatomaceous shale (oxygen-replete) deposition.

Decline of biosiliceous productivity during the Messinian salinity crisis: fact or fiction?

The Messinian sedimentary succession of the Mediterranean is typified by pre-MSC diatomaceous deposits (e.g. Pellegrino *et al.*, 2018) that are overlain by thick layers of evaporites deposited during the MSC (e.g. Roveri *et al.*, 2014). Such vertical facies transition has been traditionally regarded as the product of a sharp rise of salinity in the water column, with the consequent establishment of environmental conditions unsuitable for most marine life including biosiliceous microorganisms (e.g. Selli, 1954; Cita, 1976). However, the scattered presence of biosiliceous fossils in the MSC sedimentary record (e.g. Fourtanier *et al.*, 1991; Carnevale *et al.*, 2019; Meilijson *et al.*, 2019; Pellegrino *et al.*, 2021) suggests that biosiliceous biota persisted during the MSC. Such an interpretation is consistent with the late Miocene to early Pliocene ‘biogenic bloom’ event and the associated dramatic intensification of deposition of biogenic silica centred between 7.0 Ma and 4.5 Ma (e.g. Farrell *et al.*, 1995; Dickens & Barron, 1997; Filippelli, 1997; Dickens & Owen, 1999; Hermoyan & Owen, 2001; Cortese *et al.*, 2004; Diester-Haass *et al.*, 2002, 2004, 2005, 2006; Herbert *et al.*, 2016; Steinthorsdottir *et al.*, 2021). The hypothesis that dissolution of biogenic silica promoted the formation of authigenic clay implies that much of the MSC sedimentary record is taphonomically biased (e.g. Mancini *et al.*, 2022), preserving only a small share of the original communities of biosiliceous primary producers. In addition, the taphonomic bias hypothesis provides an alternative explanation for the anomalous abundance of smectite in the Mediterranean Messinian successions (e.g. Chamley *et al.*, 1977, 1978; Chamley & Robert, 1980; de Visser, 1991; Martínez-Ruiz *et al.*, 1999). The enrichment in smectite has been attributed to the erosion of poorly drained peri-Mediterranean soils within a semiarid Messinian climate (e.g. Chamley *et al.*, 1977; de Visser, 1991; Cosentino *et al.*, 2005), but may actually be the product of authigenic clay formation (cf. Martínez-Ruiz *et al.*, 2014) promoted by the coupling of biosiliceous productivity and intensification of water column stratification in response to the progressive isolation of the basin (e.g. Natalicchio *et al.*, 2019). Therefore, caution is advised when

interpreting the absence of skeletal remains of marine microorganisms in the sedimentary record of the MSC as evidence of their decline caused by purportedly harsh environmental conditions.

CONCLUSIONS

A multiproxy analysis of Messinian diatomaceous deposits and associated clay and dolomite-rich layers interbedded with primary gypsum deposits (Primary Lower Gypsum unit) elucidates the role of biogenic silica in authigenic clay formation during the initial stage of the Messinian salinity crisis. Anoxic bottom water conditions, induced by intensification of water column stratification, triggered silica dissolution and concomitant formation of authigenic clays and dolomite, resulting in the dolomitic mudstones of the Piedmont Basin. Organic matter remineralization was driven to a large extent by bacterial sulphate reduction. An associated increase of alkalinity induced the early diagenetic formation of dolomite, whereas the rise of pH in pore waters promoted dissolution of biogenic silica. Such biologically-induced leaching of lithogenic material under anoxic conditions promoted the partial dissolution of silicate minerals. The resultant availability of dissolved silica and reactive cations promoted the formation of authigenic clay minerals, represented by illite/smectite interlayers deriving from a smectite precursor. Absence of significant burial in the studied succession of the Piedmont Basin suggests that illitization of smectite occurred at ambient temperature and was possibly mediated by microorganisms. In contrast to periods of deposition of the dolomitic mudstones, prevailing oxygenated bottom water conditions, caused by intermittent mixing of the water column, promoted the preservation of biosiliceous remains in the diatomaceous shales. This study reinforces the hypothesis that the apparent annihilation of Mediterranean marine biota during the MSC partly reflects a taphonomic bias produced by interactions between the biogeochemical cycles of carbon, silicon and sulphur in a restricted basin rather than the establishment of adverse hypersaline conditions in the Mediterranean water mass.

FIGURE CAPTIONS

Figure 1. Geological sketch of north-west Italy. Stars highlight the two locations of the studied stratigraphic sections. TH: Torino Hill; MO: Monferrato; AM: Alto Monferrato; BG: Borbera Grue sector; SVZ: Sestri-Voltaggio zone; VVL: Villalvernia-Varzi line; IL: Insubric Line. Dashed lines indicate the isobaths of Pliocene deposits (in km). Modified from Bigi *et al.* (1990).

Figure 2. The Bric Cenciurio section. Stratigraphic log. The numbers on the left side of the stratigraphic column refer to the gypsum layers. The black arrows and numbers indicate studied samples. SKB: Sturani Key Bed.

Figure 3. Photomicrographs of diatomaceous shales from Bric Cenciurio section (samples 10 and 12; see Fig. 2). (A) Scraped surface of a hand specimen, showing the alternation of whitish, greyish, reddish and pale brown laminae; arrowheads point to gypsum aggregates. (B) Hand specimen broken parallel to the bedding plane, showing whitish, closely-stacked laminae. (C) Polished thin section, showing the alternation of opal-rich laminae (clear with n//; dark with nx) and clayey-silty laminae (dark with n//; highly birefringent with nx). (D) Partially dissolved gypsum rosettes displacing opal-rich laminae. (E) Polished thin section photomosaic; note the lateral continuity of the opal-rich laminae (darker in BSEI) and the gypsum rosettes (mostly pseudomorphs) displacing the laminated packets (arrowheads). (F) Detail of the alternation of opal-rich (dark, due to a low backscattering coefficient) and clayey-silty laminae (pale, due to high backscattering coefficient); note the excellent preservation of lamina boundary of the opal-rich laminae. (G) Detail of an opal-rich lamina, enclosing lensoidal pockets (arrowhead). (H) Detail of a clayey-silty lamina; note the diatom remains (d) and a sponge spicule (s). (A) and (B): reflected light photomicrographs; (C) and

(D): transmitted light photomicrographs (n// = parallel nicols; nx = crossed nicols); (E) to (H): BSEI photomicrographs.

Figure 4. Diatomaceous shales from Bric Cenciurio section (sample 10; see Fig. 2). Dense accumulation of: (A) and (B) Thalassionemataceae; and (C) and (D) rhizosoleniid diatoms observed along the surface of opal-rich laminae. (A) to (D): SEI photomicrographs of freshly broken chips parallel to bedding plane.

Figure 5. Diatom-bearing mudstones from Bric Cenciurio section (sample 13; see Fig. 2). (A) Scraped surface of a hand specimen showing a slight lamination; note the greyish massive layer in the lower part; white arrowheads point to gypsum crystals, pristine or partially dissolved. (B) Alternation of poorly defined, pale and reddish laminae. (C) Polished thin section photomosaic; the apparent lamination observed in reflected and transmitted light is less well-expressed, but still recognizable; arrowhead points to a gypsum grain. (D) Close-up of silt-rich laminae alternated to very thin, silt-poor laminae; arrowhead points to a pyrite framboids. (E) and (F) Details on pyrite framboids. (G) Cluster of pyrite framboid microcrystallites. (H) and (I) Centric planktonic diatoms (*Actinocyclus* cf. *octonarius* var. *tenellus*) observed in polished thin section and on a freshly broken chip cut along the bedding plane, respectively. (J) Strongly altered remain of a pennate planktonic diatom (Thalassionemataceae). (K) to (M) Remains of benthic diatoms, showing different degrees of dissolution and clay-coating; arrowhead in (L) points to the only recognizable features attributable to the diatom, otherwise almost completely clay-coated. (N) Diatom remain (left) embedded in a clayey matrix (right); note the thin thread-like structure (arrowheads). (O) Etching pits on a sponge spicule.

(A): reflected light photomicrograph; (B): transmitted light photomicrograph (n// = parallel nicols); (C) to (O): BSEI/SEI photomicrographs.

Figure 6. Dolomitic mudstones from Bric Cenciurio (samples 2, 4 and 6, see Fig. 2) and Cascina Botto sections. (A) Scraped surface of a hand specimen from Bric Cenciurio section, showing the alternation of widely- and closely-spaced laminated packets of pale and reddish laminae. (B) Scraped surface of a hand specimen from Cascina Botto section, showing well-laminated and poorly-laminated to massive packets. (C) Reddish lamina enriched in pyrite framboids (arrowheads) from Bric Cenciurio section. (D) and (E) Detail of silt-sized grains showing corroded margins and coated by a reddish halo from Bric Cenciurio section. (F) Blackish aggregate of residual organic matter (?) embedded in a dolomite-rich matrix from Bric Cenciurio section. (G) and (H) Interspersed gypsum crystals from Bric Cenciurio section. (A) and (B): reflected light photomicrograph; (C) to (H): transmitted light photomicrograph (n// = parallel nicols; nx = crossed nicols).

Figure 7. Dolomitic mudstones from Bric Cenciurio section (samples 2 and 3, see Fig. 2). (A) to (D) Finely crystalline clays closely associated with spheroidal dolomite, some of which exhibit a hollow core, observed in polished thin section and on freshly-broken chips; in D, two zoned crystals can be observed. (E) and (F) Pyrite framboids, observed in polished thin section and on freshly broken chips, respectively. (A) to (F): BSEI/SEI photomicrographs of polished thin sections and freshly-broken chips parallel to bedding plane.

Figure 8. Dolomitic mudstones from Bric Cenciurio (sample 2, see Fig. 2) and Cascina Botto sections. (A) and (B) Sponge spicule from Bric Cenciurio section (squared area is enlarged in B); note in (B) the desquamated surface of sponge spicule. (C) and (D) Sponge spicule from Cascina Botto section (squared area enlarged in D); note in (D) the etching pits on the surface of sponge spicule. (E) and (F) Almost completely dissolved benthic diatom from the Cascina Botto section. BSEI/SEI photomicrographs of freshly-broken chips parallel to bedding plane.

Figure 9. Electron dispersive X-ray spectroscopy (EDS) data points and maps of diatomaceous shales (sample 10), diatom-bearing mudstones (sample 13) and dolomitic mudstones (sample 2) from Bric Cenciurio section (see Fig. 2). Diatomaceous shales: (A) EDS data points of an opal-rich lamina of diatomaceous shale. Note the pure siliceous composition of the diatom valve. (B) and (C) Element distribution along the surface of an opal-rich lamina and a polished thin section. In the EDS maps of the polished thin section, black–blue–green–yellow–orange–red–white represent, in this order, the increasing content of each element. Diatom-bearing mudstones: (D) EDS data points of diatom valve on freshly broken chips parallel to the bedding plane. Note that diatom valves are enriched in Al, K, Fe and Mg. (E) Element distribution in a freshly broken chip cut parallel to the bedding plane. Note the enrichment in elements other than Si, in particular Al. Dolomitic mudstones: (F) EDS data points of flaky clays around dolomite crystals on freshly broken chips cut parallel to the bedding plane. (G) Element distribution along the surface of a freshly broken chip parallel to the bedding plane.

Figure 10. Al-Fe/K/Mg-Si ternary diagrams obtained from EDS analyses of diatomaceous shales (sample 10), diatom-bearing mudstones (sample 13) and dolomitic mudstones (samples 2 and 3) from Bric Cenciurio section (see Fig. 2).

Figure 11. X-ray powder diffraction (XRPD) patterns of diatomaceous shales (sample 10), diatom-bearing mudstones (sample 13) and dolomitic mudstones (sample 2 on the left, sample 3 on the right) from Bric Cenciurio section (see Fig. 2). Chl = chlorite; Dol = dolomite; Ill = illite; MxL = mixed layer clay (illite-smectite); Ox = metal oxides; Pl = plagioclase; Qz = quartz; Ver = vermiculite.

Figure 12. (A) Relative percentages of the major groups of compounds of the alcohol fraction from the diatomaceous shales, diatom-bearing and dolomitic mudstones. Samples 2, 3 and 8 are pooled

results of two extracts (see *Material and methods*). See Table 2 for the content of the major groups of compounds and Supporting Information for detailed information and contents of all measured compounds. (B) Relative percentages of the algal-derived group of compounds (sterols, diols and ketols). See Fig. 2 for the stratigraphic distribution of the samples. (C) Partial chromatogram (retention time 32–40 minutes) of the alcohol fraction after decalcification of a dolomitic mudstone (sample 2; selected mass m/z 205). MAGE: monoalkyl glycerol monoether. Note the major peak of MAGE n -C_{16:0}, which is accompanied by smaller peaks of other MAGEs ranging from 14 to 20 carbons.

Figure 13. Scenario of the water column conditions and diagenetic pathways during the deposition of dolomitic mudstones (A) and diatomaceous shales (B). The size of square and circles reflects the abundance of authigenic clays (AC), biogenic silica (BSi), dolomite (D), lithogenic material (LM), organic matter (OM) and pore water cations (PWC); bitten squares in panel (A) represent altered BSi, OM and LM. The narrow grey triangle on the left indicates oxygen penetration depth, under which bacterial sulphate reduction (BSR) is active; other biogeochemical processes like nitrate reduction, manganese reduction and iron reduction, which typically occur between the zones of aerobic respiration (above) and sulphate reduction (below) are not considered in this simplified concept. The grey arrows indicate the transport of aggregates of BSi-OM and LM from the upper water column to the sediment-water interface (SWI); white arrows in panel (B) indicate water column mixing. See text for details. The grey shade in panel A indicates progressively more oxygen-depleted waters. In panel (B), the dotted lines below the sediment-water interface indicate that the diagenetic processes involving the diatomaceous shales were less effective.

ACKNOWLEDGEMENTS

The research was supported by Fondazione Cassa di Risparmio di Torino (project n. 20192343) and grants from the University of Torino (ex-60% 2020 and 2021) to Francesco Dela Pierre.

Comments and suggestions by the Associate Editor Michael Rogerson and an anonymous reviewer greatly improved the quality of the manuscript. We warmly thank Maria Carmen Valsania

(Department of Chemistry, University of Torino) for her support during SEM analyses performed with a Tescan S9000G and Giovanna Della Porta (Department of Earth Sciences, University of Milano) for stable isotope analyses.

Accepted Article

REFERENCES

- Abe, K., Nakagawa, N., Abo, K. and Tsujino, M.** (2014) Dissolution of silica accompanied by oxygen consumption in the bottom layer of Japan's central Seto Inland Sea in summer. *J. Oceanogr.*, 70, 267-276.
- Abu-Mahfouz, I.S., Cartwright, J., Idiz, E., Hooker, J.N. and Robinson, S.A.** (2020) Silica diagenesis promotes early primary hydrocarbon migration. *Geology*, 48 (5), 483-487.
- Alfken, S., Wörmer, L., Lipp, J.S., Napier, T., Elvert, M., Wendt, J., Schimmelmann, A. and Hinrichs, K.-U.** (2021) Disrupted coherence between upwelling strength and redox conditions reflects source water change in Santa Barbara Basin during the 20th century. *Paleoceanogr. Paleoclimatol.*, 36, e2021PA004354.
- Andreotto, F., Mancini, A.M., Flecker, R., Flecker, R., Gennari, R., Lewis, J., Lozar, F., Natalicchio, M., Sangiorgi, F., Stoica, M., Dela Pierre, F. and Krijgsman, W.** (2022) Multi-proxy investigation of the post-evaporitic succession of the Piedmont Basin (Pollenzo section, NW Italy): a new piece in the Stage 3 puzzle of the Messinian Salinity Crisis. *Palaeogeogr. Palaeoclimatol. Palaeoecol.*, 594 (3), 110961.
- Andreotto, F., Aloisi, G., Raad, F., Heida, H., Flecker R., Agiadi, K., Lofi, J., Blondel, S., Bulian, F., Camerlenghi, A., Caruso, A., Ebner, R., Garcia-Castellanos, D., Gaullier, V., Guibourdenche, L., Gvirtzman, Z., Hoyle, T.M., Meijer, P.T., Moneron, J., Sierro, F.J., Travan, G., Tzevahirtzian, A., Vasiliev, I. and Krijgsman, W.** (2021) Freshening of the Mediterranean Salt Giant: controversies and certainties around the terminal (Upper Gypsum and Lago-Mare) phases of the Messinian Salinity Crisis. *Earth-Sci. Rev.*, 216 (103577), 1-47.
- Badaut, D. and Risacher, F.** (1983) Authigenic smectite on diatom frustules in Bolivian saline lakes. *Geochim. Cosmochim. Acta*, 47, 363-375.
- Behl, R.J. and Garrison, R.E.** (1994) The origin of chert in the Monterey Formation of California (USA). In: Siliceous, phosphatic and glauconitic sediments of the Tertiary and Mesozoic – Proceedings of the 29th International Geological Congress, Part C (Eds A. Ijima, A. Abed and R.E. Garrison), 101-132.
- Belias, C., Dassenakis, M. and Scoullou, M.** (2007) Study of the N, P and Si fluxes between fish farm sediment and seawater. Results of simulation experiments employing a benthic chamber under various redox conditions. *Mar. Chem.*, 103 (3-4), 266-275.

- Bellanca, A., Calderone, S. and Neri, R.** (1986) Isotope geochemistry, petrology and depositional environments of the diatomite-dominated Tripoli Formation (lower Messinian), Sicily. *Sedimentology*, 33 (5), 729-743.
- Bellanca, A., Caruso, A., Ferruzza, G., Neri, R., Rouchy, J.M., Sprovieri, M. and Blanc-Valleron, M.M.** (2001) Transition from marine to hypersaline conditions in the Messinian Tripoli Formation from the marginal areas of the central Sicilian Basin. *Sediment. Geol.*, 140, 87-105.
- Berner, R.A.** (1984) Sedimentary pyrite formation: an update. *Geochim. Cosmochim. Acta*, 48 (4), 605-615.
- Bhaskar, P.V. and Bhosle, N.B.** (2005) Microbial extracellular polymeric substances in marine biogeochemical processes. *Curr. Sci.*, 88 (1), 45-53.
- Bigi, G., Cosentino, D., Parotto, M., Sartori, R. and Scandone, P.** (1990) Structural Model of Italy: Geodynamic Project. Consiglio Nazionale delle Ricerche, S.EL.CA, scale 1:500,000, sheet 1.
- Birgel, D., Guido, A., Liu, X., Hinrichs, K.-U., Gier, S. and Peckmann, J.** (2014) Hypersaline conditions during deposition of the Calcare di Base revealed from archaeal di- and tetraether inventories. *Org. Geochem.*, 77, 11-21.
- Birnbaum, S. and Wireman, J.** (1985) Sulfate-reducing bacteria and silica solubility: a possible mechanism for evaporite diagenesis and silica precipitation in banded iron formations. *Can. J. Earth Sci.*, 22, 1904-1909.
- Bodén, P. and Backman, J.** (1996) A laminated sediment sequence from the northern North Atlantic Ocean and its climatic record. *Geology*, 24 (6), 507-510.
- Bontognali, T.R.R., Martínez-Ruiz, F., McKenzie, J.A., Bahniuk, A., Anjos, S. and Vasconcelos, C.** (2014) Smectite synthesis at low temperature and neutral pH in the presence of succinic acid. *App. Clay Sci.*, 101, 553-557.
- Bontognali, T.R.R., McKenzie, J.A., Warthmann, R.J. and Vasconcelos, C.** (2013) Microbially influenced formation of Mg-calcite and Ca-dolomite in the presence of exopolymeric substances produced by sulphate-reducing bacteria. *Terra Nova*, 26, 72-77.
- Bontognali, T.R.R., Vasconcelos, C., Warthmann, R.J., Bernasconi, S.M., Dupraz, C., Strohmengers, C.J. and McKenzie, J.A.** (2010) Dolomite formation within microbial mats in the coastal sabkha of Abu Dhabi (United Arab Emirates). *Sedimentology*, 57, 824-844.
- Brindley, G.W. and Brown, G.** (1961) The X-ray identification and crystal structures of clay minerals. London, Mineralogical Society, Clay Minerals Group, 544 pp.

- Burne, R.V., Moore, L.S., Christy, A.G., Troitzsch, U., King, P.L., Carnerup, A.M. and Hamilton, P.J.** (2014) Stevensite in the modern thrombolites of Lake Clifton, Western Australia: a missing link in microbialite mineralization? *Geology*, 42 (7), 575-578.
- Carnevale, G., Gennari, R., Lozar, F., Natalicchio, M., Pellegrino, L. and Dela Pierre, F.** (2019) Living in a deep desiccated Mediterranean Sea: an overview of the Italian fossil record of the Messinian salinity crisis. *Boll. Soc. Pal. It.*, 58, 109–140.
- Carnevale, G. and Schwarzahns, W.** (2022) Marine life in the Mediterranean during the Messinian salinity crisis: a paleoichthyological perspective. *Riv. Ital. Paleontol. Stratigr.*, 128 (2), 283-324.
- Caruso, A., Blanc-Valleron, M.M., Da Prato, S., Pierre, C. and Rouchy, J.M.** (2020) The late Messinian “Lago Mare” event and the Zanclean reflooding in the Mediterranean Sea: new insights from the Cuevas del Almanzora section (Vera Basin, South-Eastern Spain). *Earth-Sci. Rev.*, 200, 102993.
- Caruso, A., Pierre, C., Blanc-Valleron, M.M. and Rouchy, J.M.** (2015) Carbonate deposition and diagenesis in evaporitic environments: the evaporative and sulphur bearing limestones during the settlement of the Messinian salinity crisis in Sicily and Calabria. *Palaeogeogr. Palaeoclimatol. Palaeoecol.*, 429, 136-162.
- Cermeño, P.** (2016) The geological story of marine diatoms and the last generation of fossil fuels. *PIP*, 3 (2), 53-60.
- Chamley, H. and Robert, C.** (1980) Sédimentation argileuse au Tertiaire supérieur dans le domain méditerranéen. *Géol. Méditerran.*, 7 (1), 25-34.
- Chamley, H., Dunoyer de Segonzac, G. and Mélières, F.** (1978) Clay minerals in Messinian sediments of the Mediterranean area. In: *Init. Rep. DSDP* (Eds K.J. Hsü, L. Montadert, D. Bernoulli, G. Bizon, M.B. Cita, A. Erickson, F. Fabricius, R.E. Garrison, R.B. Kidd, F. Mélières, C. Müller, and R.C. Wright), 42 (1), 389-395.
- Chamley, H., Giroud d’Argoud, G. and Robert, C.** (1977) Genèse des smectites messiniennes de Sicile, implications paléoclimatiques. *Géol. Méditerran.*, 4 (4), 371-378.
- Cita, M.B.** (1976) Biodynamic effects of the Messinian salinity crisis on the evolution of planktonic foraminifera in the Mediterranean. *Palaeogeogr. Palaeoclimatol. Palaeoecol.*, 20 (1-2), 23-42.
- Cita, M.B., Wright, R.C., Ryan, W.B.F. and Longinelli, A.** (1978) Messinian paleoenvironments. In: *Init. Rep. DSDP* (Eds K.J. Hsü, L. Montadert, D. Bernoulli, G. Bizon, M.B. Cita, A. Erickson, F. Fabricius, R.E. Garrison, R.B. Kidd, F. Mélières, C. Müller, and R.C. Wright), 42 (1), 1003-1035.

- Compton, J.S.** (1991) Origin and diagenesis of clay minerals in the Monterey Formation, Santa Maria Basin area, California. *Clays and Clay Miner.*, 39, 449-466.
- Conley, D.J., Zimba, P.V. and Theriot, E.** (1990) Silica content of freshwater and marine benthic diatoms. In: *Proceedings of the 11th International Diatom Symposium* (Ed Kocielek, J.P.), 95-101.
- Cordova-Gonzalez, A., Birgel, D., Kappler, A. and Peckmann, J.** (2020) Carbon stable isotope patterns of cyclic terpenoids: A comparison of cultured alkaliphilic aerobic methanotrophic bacteria and methane-seep environments. *Org. Geochem.*, 139, 103940.
- Cortese, G., Gersonde, R., Hillenbrand, C.D. and Kuhn, G.** (2004) Opal sedimentation shifts in the World Ocean over the last 15 Ma. *Earth & Planet. Sci. Lett.*, 224, 509-527.
- Cosentino, D., Cipollari, P., Lo Mastro, S. and Giampaolo, C.** (2005) High-frequency cyclicity in the latest Messinian Adriatic foreland basin: insight into palaeoclimate and palaeoenvironments of the Mediterranean Lago-Mare episode. *Sediment. Geol.*, 178 (1-2), 31-53.
- Dählmann, A. and de Lange, G.J.** (2003) Fluid-sediment interactions at Eastern Mediterranean mud volcanoes: a stable isotope study from ODP Leg 160. *Earth & Planet. Sci. Lett.*, 212 (3-4), 377-391.
- Dale, A.W., Paul, K.M., Clemens, D., Scholz, F., Schroller-Lomnitz, U., Wallmann, K., Geilert, S., Hensen, C., Plass, A., Liebetrau, V., Grasse, P. and Sommer, S.** (2020) Recycling and burial of biogenic silica in an open margin oxygen minimum zone. *Global Biogeochem. Cycles*, 35 (2), e2020GB006583.
- Davies, R.J. and Cartwright, J.** (2002) A fossilized opal A to opal C/T transformation on the northeast Atlantic margin: support for a significantly elevated palaeogeothermal gradient during the Neogene? *Basin Res.*, 14, 467-486.
- de Lange, G.J. and Krijgsman, W.** (2010) Messinian salinity crisis: a novel unifying shallow gypsum/deep dolomite formation mechanism. *Mar. Geol.*, 275, 273-277.
- del Buey, P., Sanz-Montero, M.E., Braissant, O., Cabestrero, Ó. and Visscher, P.T.** (2021) The role of microbial extracellular polymeric substances on formation of sulfate minerals and fibrous Mg-clays. *Chem. Geol.*, 581, 120403.
- Dela Pierre, F., Bernardi, E., Cavagna, S., Clari, P., Gennari, R., Irace, A., Lozar, F., Lugli S., Manzi, V., Natalicchio, M., Roveri, M. and Violanti, D.** (2011) The record of the Messinian salinity crisis in the Tertiary Piedmont Basin (NW Italy): the Alba section revisited. *Paleogeogr. Palaeoclimatol. Palaeoecol.*, 310 (3-4), 238-255.

- Dela Pierre, F., Clari, P., Bernardi, E., Natalicchio, M., Costa, E., Cavagna, S., Lozar, F., Lugli, S., Manzi, V., Roveri, M. and Violanti, D.** (2012) Messinian carbonate-rich beds of the Tertiary Piedmont Basin (NW Italy): microbially-mediated products straddling the onset of the salinity crisis. *Palaeogeogr. Palaeoclimatol. Palaeoecol.*, 344-345, 78-93.
- Dela Pierre, F., Clari, P., Natalicchio, M., Ferrando, S., Giustetto, R., Lozar, F., Lugli, S., Manzi, V., Roveri, M. and Violanti, D.** (2014) Flocculent layers and bacterial mats in the mudstone interbeds of the Primary Lower Gypsum unit (Tertiary Piedmont Basin, NW Italy): archives of palaeoenvironmental changes during the Messinian salinity crisis. *Mar. Geol.*, 355, 71-87.
- Dela Pierre, F., Michailov, V. and Polino, R.** (1995) The tectonosedimentary evolution of the Tertiary basins in the Western Po Plain: kinematics inferred from subsidence curves. In: *Atti del Convegno "Rapporti Alpi-Appennino e guide alle escursioni"* (Eds R. Polino and R. Sacchi), Accademia Nazionale delle Scienze, 14, 129-146.
- De Rosa, M. and Gambacorta, A.** (1988) The lipids of archaeobacteria. *Prog. Lipid Res.*, 27 (3), 153–175.
- de Visser, J.P.** (1991) Clay mineral stratigraphy of Miocene to recent marine sediments in the central Mediterranean. *Geologica Ultraiectina*, 75, 244 pp.
- Di Bella, M., Italiano, F., Romano, D., Quartieri, S., Pino, P., Tripodo, A. and Sabatino, G.** (2020) Massive dolomites in the Messinian evaporitic sequence (Sicily, Italy): multi-analytical characterization and implications for the dolomitization processes. *Carbonates Evaporites*, 35 (29), 1-13.
- Dickens, G.R. and Barron, J.A.** (1997) A rapidly deposited pennate diatom ooze in upper Miocene-lower Pliocene sediment beneath the North Pacific polar front. *Mar. Micropaleontol.*, 31 (3-4), 177-182.
- Dickens, G.R. and Owen, R.M.** (1999) The latest Miocene-early Pliocene biogenic bloom: a revised Indian Ocean perspective. *Mar. Geol.*, 161 (1), 75-91.
- Dickman, M. and Glenwright, T.** (1997) A comparison of marine planktonic and sediment core diatoms in Hong Kong with emphasis on *Pseudo-nitzschia*. *Hydrobiologia*, 352, 147-156.
- Diester-Haass, L., Billups, K. and Emeis, K.C.** (2005) In search of the late Miocene-early Pliocene "biogenic bloom" in the Atlantic Ocean (Ocean Drilling Program Sites 982, 925, and 1088). *Paleoceanography*, 20 (4), 1-13.
- Diester-Haass, L., Billups, K. and Emeis, K.C.** (2006) Late Miocene carbon isotope records and marine biological productivity: was there a (dusty) link? *Paleoceanography*, 21 (4), 1-18.

- Diester-Haass, L., Meyers, P.A. and Bickert, T.** (2004) Carbonate crash and biogenic bloom in the late Miocene: evidence from ODP sites 1085, 1086, and 1087 in the Cape Basin, southeast Atlantic Ocean. *Paleoceanography*, 19 (1), 1-19.
- Diester-Haass, L., Meyers, P.A. and Vidal, L.** (2002) The late Miocene onset of high productivity in the Benguela Current upwelling system as part of a global pattern. *Mar. Geol.*, 180 (1-4), 87-103.
- Dolla, A., Fournier, M. and Dermoun, Z.** (2006) Oxygen defense in sulfate-reducing bacteria. *J. Biotechnol.*, 126 (1), 87-100.
- Dumon, M. and Van Rast, E.** (2016) PyXRD v0.6.7: a free and open-source program to quantify disordered phyllosilicates using multi-specimen X-ray diffraction profile fitting. *Geosci. Model Dev.*, 9, 41-57.
- Duverger, A., Berg, J.S., Busigny, V., Guyot, F., Bernard, S. and Miot, J.** (2020) Mechanisms of pyrite formation promoted by sulfate-reducing bacteria in pure culture. *Front. Earth Sci.*, 8:588310.
- Ehrlich, H., Demadis, K.D., Pokrovsky, O.S. and Koutsoukos, P.G.** (2010) Modern views on desilicification: biosilica and abiotic silica dissolution in natural and artificial environments. *Chem. Rev.*, 110 (8), 4656–4689.
- Ekeroth, N., Blomqvist, S. and Hall, P.O.J.** (2016) Nutrient fluxes from reduced Baltic Sea sediment: effects of oxygenation and macrobenthos. *Mar. Ecol. Prog. Ser.*, 544, 77-92.
- Elling, F.J., Hemingway, J.D., Kharbush, J.J., Becker, K.W., Polik, C.A. and Pearson, A.** (2021) Linking diatom-diazotroph symbioses to nitrogen cycle perturbations and deep-water anoxia: insights from Mediterranean sapropel events. *Earth & Planet. Sci. Lett.*, 571, 117110.
- Farrell, J.W., Raffi, I., Janecek, T.R., Murray, D.W., Levitan, M., Dadey, K.A., Emeis, K.C., Lyle, M., Flores, J.A. and Hovan, S.** (1995) Late Neogene sedimentation patterns in the Eastern Equatorial Pacific Ocean. In: *Proc. Ocean Drill. Progr. Sci. Res.* (Eds N.G. Pisias, L.A. Mayer, T.R. Janecek, A. Palmer-Julson and T. H. van Andel), 138, 717-756.
- Ferreira, A.M., Miranda, A., Caetano, M., Baas, M., Vale, C. and Sinninghe Damsté, J.S.** (2001) Formation of mid-chain alkane keto-ols by post-depositional oxidation of mid-chain diols in Mediterranean sapropels. *Org. Geochem.*, 32, 271–276.
- Filippelli, G.M.** (1997) Intensification of the Asian monsoon and a chemical weathering event in the late Miocene-early Pliocene: implications for late Neogene climate change. *Geology*, 25 (1), 27-30.

- Fourtanier, E., Gaudant, J. and Cavallo, O.** (1991) La diatomite de Castagnito (Piémont): une nouvelle preuve de l'existence d'oscillations modérées du niveau marin pendant le Messinien évaporitique. *Boll. Soc. Pal. It.*, 30 (1), 79-95.
- Friedman, G.M.** (1973) Petrographic data and comments on the depositional environment of the Miocene sulfates and dolomites at sites 124, 132 and 134, Western Mediterranean. In: *Init. Rep. DSDP* (W.B.F. Ryan, K.J. Hsü, M.B. Cita, P. Dumitrica, J.M. Lort, W. Maync, W.D. Nesteroff, G. Pautot, H. Stradner, and F.C. Wezel), 13, 695-708.
- Gallagher, K.L., Dupraz, C. and Visscher, P.T.** (2014) Two opposing effects of sulfate reduction on carbonate precipitation in normal marine, hypersaline, and alkaline environments. *Geology*, 42 (1), 313-314.
- Gallagher, K.L., Kading, T.J., Braissant, O., Dupraz, C. and Visscher, P.T.** (2012) Inside the alkalinity engine: the role of electron donors in the organomineralization potential of sulfate-reducing bacteria. *Geobiology*, 10 (6), 518-530.
- Grossi, V., Mollex, D., Vinçon-Laugier, A., Hakil, F., Pacton, M. and Cravo-Laureau, C.** (2015) Mono- and dialkyl glycerol ether lipids in anaerobic bacteria: biosynthetic insights from the mesophilic sulfate reducer *Desulfatibacillum alkenivorans* PF2803^T. *Appl. Environ. Microbiol.*, 81 (9), 3157-3168.
- Guido, A., Heindel, K., Birgel, D., Rosso, A., Mastandrea, A., Sanfilippo, R., Russo, F. and Peckmann, J.** (2013) Pendant bioconstructions cemented by microbial carbonate in submerged marine caves (Holocene, SE Sicily). *Palaeogeogr. Palaeoclimatol. Palaeoecol.*, 388, 166-180.
- Han, X., Schultz, L., Zhang, W., Zhu, J., Meng, F. and Geesey, G.G.** (2016) Mineral formation during bacterial sulfate reduction in the presence of different electron donors and carbon sources. *Chem. Geol.*, 435, 49-59.
- Haq, B., Gorini, C., Baur, J., Moneron, J. and Rubino, J.L.** (2020) Deep Mediterranean's Messinian evaporite giant: how much salt? *Glob. Planet. Change*, 184, 103052.
- Hein, J.R., Scholl, D.W., Barron, J.A., Jones, M.G. and Miller, J.** (1978) Diagenesis of late Cenozoic diatomaceous deposits and formation of the bottom simulating reflector in the southern Bering Sea. *Sedimentology*, 25, 155-181.
- Heindel, K., Birgel, D., Brunner, B., Thiel, V., Westphal, H., Gischler, E., Ziegenbalg, S.B., Cabioch, G., Sjövall, P. and Peckmann, J.** (2012) Post-glacial microbialite formation in coral reefs of the Pacific, Atlantic, and Indian Oceans. *Chem. Geol.*, 304-305, 117-130.

- Hemingway, J.D., Schefuß, E., Dinga, B.J., Pryer, H. and Galy, V.V. (2016)** Multiple plant-wax compounds record differential sources and ecosystem structure in large river catchments. *Geochim. et Cosmochim. Acta*, 184, 20-40.
- Herbert, T.D., Lawrence, K.T., Tzanova, A., Cleaveland Peterson, L., Caballero-Gill, R. and Kelly, C.S. (2016)** Late Miocene global cooling and the rise of modern ecosystems. *Nat. Geosci.*, 9, 843-847.
- Hermoyian, C.S. and Owen, R.M. (2001)** Late Miocene-early Pliocene biogenic bloom: evidence from low-productivity regions of the Indian and Atlantic Oceans. *Paleoceanography*, 16 (1), 95-100.
- Hiebert, F.K. and Bennett, P.C. (1992)** Microbial control of silicate weathering in organic-rich ground water. *Science*, 258 (5080), 278-281.
- Hinrichs, K.-U., Summons, R.E., Orphan, V., Sylva, S.P. and Hayes, J.M. (2000)** Molecular and isotopic analysis of anaerobic methane-oxidizing communities in marine sediments. *Org. Geochem.*, 31 (12), 1685-1701.
- Hoffmann-Sell, L., Birgel, D., Arning, E.T., Föllmi, K.B. and Peckmann, J. (2011)** Archaeal lipids in Neogene dolomites (Monterey and Sisquoc Formations, California) - Planktic versus benthic archaeal sources. *Org. Geochem.*, 42 (6), 593-604.
- Holstein, J.M. and Hensen, C. (2009)** Microbial mediation of benthic biogenic silica dissolution. *Geo-Mar. Lett.*, 30, 477-492.
- Howell, J.R., Donahoe, R.J., Roden, E.E. and Ferris, F.G. (1998)** Effects of microbial iron oxide reduction on pH and alkalinity in anaerobic bicarbonate-buffered media: implications for metal mobility. *Goldschmidt Conference, Toulouse*, 657-658.
- Hsü, K.J., Ryan, W.B.F. and Cita, M.B. (1973)** Late Miocene dessication of the Mediterranean. *Nature*, 242, 240-244.
- Huggett, J., Hooker, J.N. and Cartwright, J. (2017)** Very early diagenesis in a calcareous, organic-rich mudrock from Jordan. *Arab. J. Geosci.*, 10, 270, 1-12.
- Hüsing, S.K., Kuiper, K.F., Link, W., Hilgen, F.J. and Krijgsman, W. (2009)** The upper Tortonian-lower Messinian at Monte dei Corvi (Northern Apennines, Italy): completing a Mediterranean reference section for the Tortonian Stage. *Earth Planet. Sci.*, 282 (1-4), 140-157.
- Irace, A., Dela Pierre, F. and Clari, P. (2005)** «Normal» and «chaotic» deposits in the Messinian Gessoso-solfifera Fm. at the north-eastern border of the Langhe domain (Tertiary Piedmont basin). *Boll. Soc. Geol. Ital.*, 4, 77-85.

- Isaji, Y., Kawahata, H., Takano, Y., Ogawa, N.O., Kuroda, J., Yoshimura, T., Lugli, S., Manzi, V., Roveri, M. and Ohkouchi, N.** (2019) Diazotrophy drives primary production in organic-rich shales deposited under a stratified environment during the Messinian salinity crisis (Vena del Gesso, Italy). *Front. Earth Sci.*, 7, 85, 1-13.
- Jørgensen, B.B., Wenzhöfer, F., Egger, M. and Glud, R.N.** (2022) Sediment oxygen consumption: role in the global marine carbon cycle. *Earth-Sci. Rev.*, 103987.
- Jurkowska, A., Świerczewska-Gładysz, E., Bąk, M. and Kowalik, S.** (2019) The role of biogenic silica in the formation of Upper Cretaceous pelagic carbonates and its palaeoecological implications. *Cretac. Res.*, 93, 170-187.
- Kelts K. and McKenzie, J.** (1984) A comparison of anoxic dolomite from deep-sea sediments: Quaternary Gulf of California and Messinian Tripoli Formation of Sicily. In: *Dolomites of the Monterey Formation and other organic-rich units* (Eds R.E. Garrison, M. Kastner, D.H. Zenger), Pacific Section SEPM, 41, 19-28.
- Kemp, A.E.S. and Baldauf, J.G.** (1993) Vast Neogene laminated diatom mat deposits from the eastern equatorial Pacific Ocean. *Nature*, 362, 141-144.
- Kemp, A.E.S., Pearce, R.B., Koizumi, I., Pike, J. and Rance, S.J.** (1999) The role of mat-forming diatoms in the formation of Mediterranean sapropels. *Nature*, 398, 57-61.
- Kemp, A.E.S., Pearce, R.B., Pike, J. and Marshall, J.E.A.** (1998) Microfabric and microcompositional studies of Pliocene and Quaternary sapropels from the eastern Mediterranean. In: *Proc. Ocean Drill. Progr. Sci. Res.* (Eds A.H.F., Robertson, K.C. Emeis, C. Richter, A. Camerlenghi, A.), 160, 333-348.
- Kemp, A.E.S., Pike, J., Pearce, R.B. and Lange, C.B.** (2000) The “fall dump” – a new perspective on the role of a “shade flora” in the annual cycle of diatom production and export flux. *Deep-Sea Res. II: Top. Stud. Oceanogr.*, 47 (9-11), 2129-2154.
- Kim, J., Dong, H., Seabaugh, J., Newell, S.W. and Eberl, D.D.** (2004) Role of microbes in the smectite-to-illite reaction. *Science*, 303, 830-832.
- Kim, J., Dong, H., Yang, K., Park, H., Elliott W.C., Spivack, A., Koo, T., Kim, G., Morono, Y., Henkel, S., Inagaki, F., Zeng, Q., Hoshino, T. and Heuer, V.B.** (2019) Naturally occurring, microbially induced smectite-to-illite reaction. *Geology*, 47 (6), 535-539.
- Kim, S.T., Coplen, T.B. and Horita, J.** (2015) Normalization of stable isotope data for carbonate minerals: Implementation of IUPAC guidelines. *Geochim. Cosmochim. Acta*, 158, 276–289.

- Koizumi, I. and Yamamoto, H. (2018)** Diatom ooze and diatomite-diatomaceous sediments in and around the North Pacific Ocean. *JAMSTEC Report of Research and Development*, 27, 26-46.
- Konhauser, K.O. and Urrutia, M.M. (1999)** Bacterial clay authigenesis: a common biogeochemical process. *Chem. Geol.*, 161 (4), 399-413.
- Kouwenhoven, T.J. and van der Zwaan, G.J. (2006)** A reconstruction of late Miocene Mediterranean circulation patterns using benthic foraminifera. *Palaeogeogr. Palaeoclimatol. Palaeoecol.*, 238 (1-4), 373-385.
- Kremer, B., Kaźmierczak, J. and Kempe, S. (2019)** Authigenic replacement of cyanobacterially precipitated calcium carbonate by aluminium-silicates in giant microbialites of Lake Van (Turkey). *Sedimentology*, 66 (1), 285-304.
- Kremer, B., Kaźmierczak, J. and Środoń, J. (2018)** Cyanobacterial-algal crusts from Late Ediacaran paleosols of the East European Craton. *Precambrian Res.*, 305, 236-246.
- Krijgsman, W., Hilgen, F.J., Raffi, I., Sierro, F.J. and Wilson, D.S. (1999)** Chronology, causes and progression of the Messinian salinity crisis. *Nature*, 400, 652-655.
- Lehtimäki, M., Sinkko, H. and Tallberg, P. (2016)** The role of oxygen conditions in the microbial dissolution of biogenic silica under brackish conditions. *Biogeochemistry*, 129 (3), 355–371.
- Li, M., Wignall, P.B., Dai, X., Hu, M. and Song, H. (2021)** Phanerozoic variation in dolomite abundance linked to oceanic anoxia. *Geology*, 49 (6), 698-702.
- Lin, Z., Sun, X., Lu, Y., Xu, L., Gong, J., Lu, H., Teichert, B.M.A. and Peckmann, J. (2016)** Stable isotope patterns of coexisting pyrite and gypsum indicating variable methane flow at a seep site of the Shenhu area, South China Sea. *J. Asian Earth Sci.*, 123, 213-223.
- Lindtke, J., Ziegenbalg, S.B., Brunner, B., Rouchy, J.M., Pierre, C. and Peckmann, J. (2011)** Authigenesis of native sulphur and dolomite in a lacustrine evaporitic setting (Hellin basin, Late Miocene, SE Spain). *Geol. Mag.* 148 (4), 655-669.
- Liu, D., Dong, H., Bishop, M.E., Zhang, J., Wang, H., Xie, S., Wang, S., Huang, L. and Eberl, D.D. (2012)** Microbial reduction of structural iron in interstratified illite-smectite minerals by a sulfate-reducing bacterium. *Geobiology*, 10 (2), 150-162.
- Londry, K.L. and Des Marais, D.J. (2003)** Stable carbon isotope fractionation by sulfate-reducing bacteria. *Appl. Environ. Microb.*, 69 (5), 2942-2949.
- Lozar, F., Violanti, D., Bernardi, E., Dela Pierre, F. and Natalicchio, M. (2018)** Identifying the onset of the Messinian salinity crisis: a reassessment of the biostratigraphic tools (Piedmont Basin, NW Italy). *Newsl. Stratigr.*, 51 (1), 11-31.

- Lu, Y., Sun, X., Xu, H., Konishi, H., Lin, Z., Xu, L., Chen, T., Hao, X., Lu, H. and Peckmann, J.** (2018) Formation of dolomite catalyzed by sulfate-driven anaerobic oxidation of methane: Mineralogical and geochemical evidence from the northern South China Sea. *Am. Min.*, 103 (5), 720-734.
- Lu, Y., Yang, X., Lin, Z., Sun, X., Yang, Y. and Peckmann, J.** (2021) Reducing microenvironments promote the incorporation of magnesium ions into authigenic carbonate forming at methane seeps: Constraints for dolomite formation. *Sedimentology*, 68 (7), 2945-2964.
- Mancini, A.M., Gennari, R., Natalicchio, M., Dela Pierre, F., Carnevale, L., Pastero, L., Pellegrino, L., Pilade, F. and Lozar, F.** (2022) Taphonomic bias on calcareous micro and nanofossils and paleoenvironmental evolution across the Messinian salinity crisis onset: insights from the Sorbas Basin (SE Spain). *Palaeogeogr. Palaeoclimatol. Palaeoecol.*, 599, 111056.
- Manzi, V., Lugli, S., Ricci Lucchi, F. and Roveri, M.** (2005) Deep-water clastic evaporites deposition in the Messinian Adriatic foredeep (northern Apennines, Italy): did the Mediterranean ever dry out? *Sedimentology*, 52, 875-902.
- Manzi, V., Roveri, M., Argnani, A., Cowan, D. and Lugli, S.** (2021) Large-scale mass-transport deposits recording the collapse of an evaporitic platform during the Messinian salinity crisis (Caltanissetta basin, Sicily). *Sediment. Geol.*, 424, 106003.
- Martínez-Ruiz, F., Comas, M., Vasconcelos, C.** (2014) Clay mineral assemblage as proxies for reconstructing Messinian paleoenvironments in the western Mediterranean. EGU General Assembly 2014, Vienna, Austria.
- Martínez-Ruiz, F., Comas, M.C. and Alonso, B.** (1999) Mineral associations and geochemical indicators in Upper Miocene to Pleistocene sediments in the Alboran Basin. In: *Proc. Ocean Drill. Progr. Sci. Res.* (Eds R. Zahn, M.C. Comas and A. Klaus), 161, 21-36.
- Mazzullo, S.J.** (2000) Organogenic dolomitization in peritidal to deep-sea sediments. *J. Sediment. Res.*, 70 (1), 10-23.
- McKenzie, J.A., Jenkyns, H.C. and Bennett, G.G.** (1979) Stable isotope study of the cyclic diatomite-claystones from the Tripoli Formation, Sicily: a prelude to the Messinian salinity crisis. *Palaeogeogr. Palaeoclimatol. Palaeoecol.*, 29, 125-141.
- McKirdy, D.M., Spiro, B., Kim, A.W., Brenchley, A.J., Hepplewhite, C.J. and Mazzoleni, A.G.** (2013) Environmental significance of mid- to late Holocene sapropels in Old Man Lake, Coorong coastal plain, South Australia: an isotopic, biomarker and palaeoecological perspective. *Org. Geochem.*, 58, 13-26.

- Meilijson, A., Hilgen, F., Sepúlveda, J., Steinberg, J., Fairbank, V., Flecker, R., Waldmann, N.D., Spaulding, S.A., Bialik, O.M., Boudinot, F.G., Illner, P. and Makovsky, Y.** (2019) Chronology with a pinch of salt: integrated stratigraphy of Messinian evaporites in the deep Eastern Mediterranean reveals long-lasting halite deposition during Atlantic connectivity. *Earth-Sci. Rev.*, 194, 374-398.
- Michalopoulos, P. and Aller, R.C.** (1995) Rapid clay mineral formation in Amazon Delta sediments: reverse weathering and oceanic elemental cycles. *Science*, 270 (5236), 614-617.
- Michalopoulos, P. and Aller, R.C.** (2004) Early diagenesis of biogenic silica in the Amazon Delta: alteration, authigenic clay formation, and storage. *Geochim. Cosmochim. Acta*, 68 (5), 1061-1085.
- Mosca, P., Polino, R., Rogledi, S. and Rossi, M.** (2010) New data for the kinematic interpretation of the Alps-Appennines junction (Northwestern Italy). *Int. J. Earth Sci.*, 99 (4), 833-849.
- Muza, J.P. and Sherwood, W.W. Jr** (1983) An authigenic gypsum, pyrite, and glauconite association in a Miocene deep sea biogenic ooze from the Falkland Plateau, Southwest Atlantic Ocean. In: *Init. Rep. DSDP* (Eds W.J. Ludwig, V.A. Krasheninnikov, W.W. Jr Sherwood), 71, 361-375.
- Natalicchio, M., Birgel, D., Peckmann, J., Lozar, F., Carnevale, G., Liu, X.L., Hinrichs, K.-U. and Dela Pierre, F.** (2017) An archaeal biomarker record of paleoenvironmental change across the onset of the Messinian salinity crisis in the absence of evaporites (Piedmont Basin, Italy). *Org. Geochem.*, 113, 242-253.
- Natalicchio, M., Dela Pierre, F., Birgel, D., Brumsack, H., Carnevale, G., Gennari, R., Gier, S., Lozar, F., Pellegrino, L., Sabino, M., Schmetger, B. and Peckmann, J.** (2019) Paleoenvironmental change in a precession-paced succession across the onset of the Messinian salinity crisis: insight from element geochemistry and molecular fossils. *Palaeogeogr. Palaeoclimatol. Palaeoecol.*, 518, 45-61.
- Natalicchio, M., Pellegrino, L., Clari, P., Pastoro, L. and Dela Pierre, F.** (2021) Gypsum lithofacies and stratigraphic architecture of a Messinian marginal basin (Piedmont Basin, NW Italy). *Sediment. Geol.*, 425, 106009.
- Neumeister, S., Misch, D., Algeo, T.J., Gawlick, H.J., Gratzner, R. and Sachsenhofer, R.F.** (2020) Early diagenesis of organic-rich marls under shifting suboxic to euxinic conditions: the lower Toarcian of the Bächental basin. *Mar. Pet. Geol.*, 120, 104513.
- Noël, D. and Rouchy, J.M.** (1986) Transformations minerals in situ de frustules de diatomées du Miocène d'Égypte. Double voie de la diagenèse : silicification et argilogenèse. *C. R. Acad. Sci.*, 303 (II) 19, 1743-1748.

- Ogniben, L.** (1957) Petrografia della serie solfifera siciliana e considerazioni geologiche relative. Memorie descrittive della Carta Geologica d'Italia 33, Libreria dello Stato, Roma, 275 pp.
- Pearce, R.B., Kemp, A.E.S., Koizumi, I., Pike, J., Cramp, A. and Rowland, S.J.** (1998) A lamina-scale, SEM-based study of a late Quaternary diatom-ooze sapropel from the Mediterranean Ridge, site 971. In: Proc. Ocean Drill. Progr. Sci. Res. (Eds A.H.F. Robertson, K.C. Emeis, C. Richter and A. Camerlenghi), 160, 349-363.
- Pellegrino, L., Abe, K., Gennari, R., Lozar, F., Dela Pierre, F., Natalicchio, M., Mikami, Y., Jordan, R.W. and Carnevale, G.** (2020a) Integrated micropaleontological study of the Messinian diatomaceous deposits of the Monferrato Arc (Piedmont basin, NW Italy): new insights into the paleoceanographic evolution of the northernmost Mediterranean region. *Mar. Micropal.*, 160, 101910.
- Pellegrino, L., Dela Pierre, F., Jordan, R.W., Abe, K., Mikami, Y., Natalicchio, M., Gennari, R., Lozar, F. and Carnevale, G.** (2020b) The upper Miocene diatomaceous sediments of the northernmost Mediterranean region: a lamina-scale investigation of an overlooked palaeoceanographic archive. *Sedimentology*, 67 (7), 3389-3421.
- Pellegrino, L., Dela Pierre, F., Natalicchio, M. and Carnevale, G.** (2018) The Messinian diatomite deposition in the Mediterranean region and its relationships to the global silica cycle. *Earth-Sci. Rev.*, 178, 154-176.
- Pellegrino, L., Natalicchio, M., Abe, K., Jordan, R.W., Favero Longo, S.E., Ferrando, S., Carnevale, G. and Dela Pierre, F.** (2021) Tiny, glassy, and rapidly trapped: the nano-sized planktic diatoms in Messinian (late Miocene) gypsum. *Geology*, 49, (11), 1369-1374.
- Pérez-Folgado, M., Sierro, F.J., Bárcena, M.A., Flores, J.A., Vázquez, A., Utrilla, R., Hilgen, F.J., Krijgsman, W. and Filippelli, G.M.** (2003) Western versus eastern Mediterranean paleoceanographic response to astronomical forcing: a high-resolution microplankton study of precession-controlled sedimentary cycles during the Messinian. *Palaeo. Palaeo. Palaeo.*, 190, 317-334.
- Petranich, E., Covelli, S., Acquavita, A., De Vittor, C., Faganelli, J. and Contin, M.** (2018) Benthic nutrient cycling at the sediment-water interface in a lagoon fish farming system (northern Adriatic Sea, Italy). *Sci. Total Environ.*, 644, 137–149.
- Petrash, D.A., Bialik, O.M., Bontognali, T.R.R., Vasconcelos, C., Roberts, J.A., McKenzie, J.A. and Konhauser, K.O.** (2017) Microbially catalyzed dolomite formation: from near-surface to burial. *Earth-Sci. Rev.*, 171, 558-582.

- Pierella Karlusich, J.J., Bowler, C. and Biswas, H. (2021)** Carbon dioxide concentration mechanisms in natural populations of marine diatoms: insights from *Tara* Oceans. *Front. Plant Sci.*, 12 (657821), 1-19.
- Pierre, C., Rouchy, J.M. and Blanc-Valleron, M.M. (2002)** Gas hydrate dissociation in the Lorca Basin (SE Spain) during the Mediterranean Messinian salinity crisis. *Sediment. Geol.*, 147 (3-4), 247-252.
- Pike, J. and Kemp, A.E.S. (1999)** Diatom mats in Gulf of California sediments: implications for the paleoenvironmental interpretation of laminated sediments and silica burial. *Geology*, 27 (4), 311-314.
- Pisciotta, K. (1981)** Diagenetic trends in the siliceous facies of the Monterey Shale in the Santa Maria region, California. *Sedimentology*, 28 (4), 547-571.
- Pollastro, R.M. (1990)** The illite/smectite geothermometer – Concepts, methodology, and application to basin history and hydrocarbon generation. In: *Applications of thermal maturity studies to energy exploration* (Eds V.F. Nuccio, and C.E. Barker), Rocky Mountain Section SEPM, 1-18.
- Presti, M. and Michalopoulos, P. (2008)** Estimating the contribution of the authigenic mineral component to the long-term reactive silica accumulation on the western shelf of the Mississippi River Delta. *Cont. Shelf Res.*, 28 (6), 823-838.
- Rahman, S. (2019)** Reverse weathering reactions in marine sediments. *Reference Module in Earth Systems and Environmental Sciences – Encyclopedia of Ocean Sciences (Third Edition)*, 4, 216-227.
- Rampen, S.W., Abbas, B.A., Schouten, S. and Sinninghe Damsté, J.S. (2010)** A comprehensive study of sterols in marine diatoms (Bacillariophyta): implications for their use as tracers for diatom productivity. *Limnol. Oceanogr.*, 55, 91-105.
- Rampen, S.W., Friedl, T., Rybalka, N. and Thiel, V. (2022)** The long chain diol index: a marine palaeotemperature proxy based on eustigmatophyte lipids that record the warmest seasons. *Proc. Nat. Acad. Sci. USA*, 119 (16), e2116812119.
- Rommerskirchen, F., Plader, A., Eglinton, G., Chikaraishi, Y. and Rullkötter, J. (2006)** Chemotaxonomic significance of distribution and stable carbon isotopic composition of long-chain alkanes and alkan-1-ols in C₄ grass waxes. *Org. Geochem.*, 37, 1303–1332.
- Rossi, M. (2017)** Outcrop and seismic expression of stratigraphic patterns driven by accommodation and sediment supply turnarounds: implications on the meaning and variability of unconformities in syn-orogenic basins. *Mar. Pet. Geol.*, 87, 112–127.

- Rossi, M. and Craig, J.** (2016) A new perspective on sequence stratigraphy of syn-orogenic basins: insights from the Tertiary Piedmont Basin (Italy) and implications for play concepts and reservoir heterogeneity. In: The value of outcrop studies in reducing subsurface uncertainty and risk in hydrocarbon exploration and production (Eds M. Bowman, H.R. Smyth, T.R. Good, S.R. Passey, J.P.P. Hirst, and C.J. Jordan), Geol. Soc. Spec. Publ., 436 (1), 93-133.
- Rouchy, J.M. and Caruso, A.** (2006) The Messinian salinity crisis in the Mediterranean basin: a reassessment of the data and an integrated scenario. *Sediment. Geol.*, 188-189, 35-67.
- Roveri, M., Flecker, R., Krijgsman, W., Lofi, J., Lugli, S., Manzi, V., Sierro, F.J., Bertini, A., Camerlenghi, A., De Lange, G., Govers, R., Hilgen F.J., Hübscher, C., Meijer, P.T. and Stoica, M.** (2014) The Messinian salinity crisis: past and future of a great challenge for marine sciences. *Mar. Geol.*, 352, 25-58.
- Rütters, H., Sass, H., Cypionka, H. and Rullkötter, J.** (2001) Monoalkylether phospholipids in the sulfate-reducing bacteria *Desulfosarcina variabilis* and *Desulforhabdus amnigenus*. *Arch. Microbiol.*, 176, 435-442.
- Ryan, W.B.F.** (1973) Geodynamic implications of the Messinian crisis of salinity. In: Messinian events in the Mediterranean (Ed C.W. Drooger), North Holland Publication Company, Amsterdam, pp. 26-38.
- Sabino, M., Dela Pierre, F., Natalicchio, M., Birgel, D., Gier, S. and Peckmann, J.** (2021) The response of water column and sedimentary environments to the advent of the Messinian salinity crisis: insights from an onshore deep-water section (Govone, NW Italy). *Geol. Mag.*, 158 (5), 825-841.
- Sanz-Montero, M.E., Rodríguez-Aranda, J.P. and Pérez-Soba, C.** (2009) Microbial weathering of Fe-rich phyllosilicates and formation of pyrite in the dolomite precipitating environment of a Miocene lacustrine system. *Eur. J. Mineral.*, 21 (1), 163-175.
- Schulz, H., Von Rad, U. and Von Stackelberg, U.** (1996) Laminated sediments from the oxygen-minimum zone of the northeastern Arabian Sea. In: Palaeoclimatology and palaeoceanography from laminated sediments (Ed A.E.S. Kemp), Palaeoclimatology and palaeoceanography from laminated sediments, Geol. Soc. Spec. Publ., 116, 185-207.
- Schwark, L., Ferretti, A., Papazzoni, C.A. and Trevisani, E.** (2009) Organic geochemistry and paleoenvironment of the Early Eocene “Pesciara di Bolca” Konservat-Lagerstätte, Italy. *Palaeo. Palaeo. Palaeo.*, 273 (3), 272-285.
- Selli, R.** (1954) Il bacino del Metauro – Descrizione geologica, risorse minerarie, idrogeologia. Cassa di Risparmio di Fano, 254 pp.

- Selli, R.** (1973) An outline of the Italian Messinian. In: Messinian events in the Mediterranean (Ed C.W. Drooger), North Holland Publication Company, Amsterdam, pp. 150-171.
- Shimada, C., Sato, T., Toyoshima, S., Yamasaki, M. and Tanimura, Y.** (2008) Paleoecological significance of laminated diatomaceous oozes during the middle-to-late Pleistocene, North Atlantic Ocean (IODP Site U1304). *Mar. Micropal.*, 69 (2), 139-150.
- Shoonen, M.A.A.** (2004) Mechanisms of sedimentary pyrite formation. *Geol. Soc. Am. Spec. Pap.*, 379, 117-134.
- Siipola, V., Lehtimäki, M. and Tallberg, P.** (2016) The effects of anoxia on Si dynamics in sediments. *J. Soils Sediments*, 16 (1), 266-279.
- Silburn, B., Kröger, S., Parker, E.R., Sivyer, D.B., Hicks, N., Powell, C.F., Johnson, M. and Greenwood, N.** (2017) Benthic pH gradients across a range of shelf sea sediment types linked to sediment characteristics and seasonal variability. *Biogeochemistry*, 135, 69-88.
- Sinninghe Damsté, J.S., Frewin, N.L., Kenig, F. and de Leeuw, J.W.** (1995) Molecular indicators for palaeoenvironmental change in a Messinian evaporitic sequence (Vena del Gesso, Italy). I: variations in extractable organic matter of ten cyclically deposited marl beds. *Org. Geochem.*, 23 (6), 471-483.
- Sinninghe Damsté, J.S., Rampen, S., Rijpstra, W.I.C., Abbas, B., Muyzer, G. and Schouten, S.** (2003) A diatomaceous origin for long-chain diols and mid-chain hydroxy methyl alkanolates widely occurring in Quaternary marine sediments: indicators for high nutrient conditions. *Geochim. Cosmochim. Acta*, 67 (7), 1339–1348.
- Smrzka, D., Kraemer, S.M., Zwicker, J., Birgel, D., Fischer, D., Kasten, S., Goedert, J.L. and Peckmann, J.** (2015) Constraining silica diagenesis in methane-seep deposits. *Palaeogeogr. Palaeoclimatol. Palaeoecol.*, 420, 13-26.
- Souchu, P., Gasc, A., Collos, Y., Vaquer, A., Tournier, H., Bibent, B. and Deslous-Paoli, J.M.** (1998) Biogeochemical aspects of bottom anoxia in a Mediterranean lagoon (Thau, France). *Mar. Ecol. Prog. Ser.*, 164, 135-146.
- Spagnoli, F. and Bergamini, M.C.** (1997) Water-sediment exchange of nutrients during early diagenesis and resuspension of anoxic sediments from the Northern Adriatic Sea shelf. *Wat. Air and Soil Poll.*, 99, 541-556.
- Steinthorsdottir, M., Coxal, H.K., de Boer, A.M., Huber, M., Barbolini, N., Bradshaw, C.D., Burls, N.J., Feakins, S.J., Gasson, E., Henderiks, J., Holbourn, A.E., Kiel, S., Kohn, M.J., Knorr, G., Kürschner, W.M., Lear, C.H., Liebrand, D., Lunt, D.J., Mörs, T., Pearson, P.N., Pound, M.J., Stoll, H. and Strömberg, C.A.E.** (2021) The Miocene: the future of the past. *Paleoceanogr. Paleoclimatol.*, 36 (4), e2020PA004037.

- Sturani, C. and Sampò, M.** (1973) Il Messiniano inferiore in facies diatomitica nel Bacino Terziario Piemontese. *Mem. Soc. Geol. It.*, 12, 335-358.
- Thyberg, B.I., Stabell, B., Faleide, J.I. and Bjørlykke, K.** (1999) Upper Oligocene diatomaceous deposits in the northern North Sea – silica diagenesis and paleogeographic implications. *Norw. J. Geol.*, 79, 3-18.
- Tréguer, P.J., Bowler, C., Moriceau, B., Dutkiewicz, S., Gehlen, M., Aumont, O., Bittner, L., Dugdale, R., Finkel, Z., Iudicone, D., Jahn, O., Guidi, L., Lasbleiz, M., Leblanc, K., Levy, M. and Pondaven, P.** (2018) Influence of diatom diversity on the ocean biological carbon pump. *Nat. Geosci.*, 11, 23-37.
- Tréguer, P.J., Sutton, J.N., Brzezinski, M., Charette, M.A., Devries, T., Dutkiewicz, S., Ehlert, C., Hawkings, J., Leynaert, A., Liu, S.M., Llopis Monferrer, N., López-Acosta, M., Maldonado, M., Rahman, S., Ran, L. and Rouxel, O.** (2021) Reviews and syntheses: the biogeochemical cycle of silicon in the modern ocean. *Biogeosciences*, 18, 1269-1289.
- Tribovillard, N., Bout-Roumazielles, V., Delattre, M., Ventalon, S. and Bensadok, A.** (2022) Sedimentary pyrite as a trap of organic matter: preliminary results from large-framboid observation. *Eur. J. Mineral.*, 34, 77-83.
- Tzevahirtzian, A., Caruso, A., Scopelliti, G., Baudin, F. and Blanc-Valleron, M.M.** (2022) Onset of the Messinian Salinity Crisis: sedimentological, petrographic and geochemical characterization of the pre-salt sediments from a new core (Caltanissetta Basin, Sicily). *Mar. Pet. Geol.*, 141, 105686.
- Ullman, W.J., Kirchman, D.L., Welch, S.A. and Vandevivere, P.** (1996) Laboratory evidence for microbially mediated silicate mineral dissolution in nature. *Chem. Geol.*, 132 (1-4), 11-17.
- van der Lingen, G.J.** (1977) Diagenesis of deep-sea biogenic sediments. *Benchmark Papers in Geology* 40, Dowden, Hutchinson & Ross, Inc, 385 pp.
- Varkouhi, S., Tosca, N. and Cartwright, J.A.** (2021) Temperature-time relationships and their implications for thermal history and modelling of silica diagenesis in deep-sea sediments. *Mar. Geol.*, 439, 106541.
- Vasconcelos, C., McKenzie, J.A., Bernasconi, S., Grujic, D. and Tiens, A.J.** (1995) Microbial mediation as a possible mechanism for natural dolomite formation at low temperatures. *Nature*, 377, 220-222.
- Versteegh, G.J.M., Bosch, H.J. and De Leeuw, J.W.** (1997) Potential palaeoenvironmental information of C₂₄ to C₃₆ mid-chain diols, keto-ols and mid-chain hydroxy fatty acids; a critical review. *Org. Geochem.*, 27, 1-13.

- Villnäs, A., Norkko, J., Lukkari, K., Hewitt, J. and Norkko, A.** (2012) Consequences of increasing hypoxic disturbance on benthic communities and ecosystem functioning. *PLoS ONE*, 7 (10), e44920.
- Vinçon-Laugier, A., Grossi, V., Pacton, M., Escarguel, G. and Cravo-Laureau, C.** (2016) The alkyl glycerol ether lipid composition of hereotrophic sulfate reducing bacteria strongly depends on growth substrate. *Org. Geochem.*, 98, 141-154.
- Volkman, J.K. and Hallegraeff, G.M.** (1988) Lipids in marine diatoms of the genus *Thalassiosira*: Predominance of 24-methylenecholesterol. *Phytochemistry*, 27, 1389–1394.
- Volkman, J.K., Barrett, S.M. and Blackburn, S.I.** (1999) Eustigmatophyte microalgae are potential sources of C₂₉ sterols, C₂₂–C₂₈ *n*-alcohols and C₂₈–C₃₂ *n*-alkyl diols in freshwater environments. *Org. Geochem.*, 30 (5), 307–318.
- Volkman, J.K., Barrett, S.M., Blackburn, S.I., Mansour, M.P., Sikes, E.L. and Gelin, F.** (1998) Microalgal biomarkers: A review of recent research developments. *Org. Geochem.*, 29 (5-7), 1163–1179.
- Volkman, J.K., Barrett, S.M., Dunstan, G.A. and Jeffrey, S.W.** (1993) Geochemical significance of the occurrence of dinosterol and other 4-methyl sterols in a marine diatom. *Org. Geochem.*, 20 (1), 7-15.
- Warren, J.** (2000) Dolomite: occurrence, evolution and economically important associations. *Earth-Sci. Rev.*, 52 (1-3), 1-81.
- Werne, J. P., Baas, M. and Sinninghe Damsté, J. S.** (2002) Molecular isotopic tracing of carbon flow and trophic relationships in a methane-supported benthic microbial community. *Limnol. Oceanogr.*, 47 (6), 1694-1701.
- Westacott, S., Planavsky, N.J., Zhao, M.Y. and Hull, P.M.** (2021) Revisiting the sedimentary record of the rise of diatoms. *Proc. Nat. Acad. Sci. U.S.A.*, 118 (27), e2103517118.
- White, L.D., Garrison, R.E. and Barron, J.A.** (1992) Miocene intensification of upwelling along the California margin as recorded in siliceous facies of the Monterey Formation and offshore DSDP sites. In: *Upwelling systems: evolution since the early Miocene* (Eds C.P. Summerhayes, W.L. Prell K.C. Emeis), *Geol. Soc. Spec. Publ.*, 64, 429–442.
- Wilkin, R.T., Barnes, H.L. and Brantley, S.L.** (1996) The size distribution of framboidal pyrite in modern sediments: an indicator of redox conditions. *Geochim. Cosmochim. Acta*, 60 (20), 3897-3912.
- Wilson, M.J., Shaldybin, M.V. and Wilson, L.** (2016) Clay mineralogy and unconventional hydrocarbon shale reservoirs in the USA. I. Occurrence and interpretation of mixed-layer R3 ordered illite/smectite. *Earth. Sci. Rev.*, 158, 31-50.

- Wojdyr, M.** (2010) Fityk: a general-purpose peak fitting program. *J. Appl. Crystallogr.*, 43 (5), 1126-1128.
- Wright, D.T.** (1999) The role of sulphate-reducing bacteria and cyanobacteria in dolomite formation in distal ephemeral lakes of the Coorong region, South Australia. *Sediment. Geol.*, 126, 147-157.
- Wright, D.T. and Wacey, D.** (2005) Precipitation of dolomite using sulphate-reducing bacteria from the Coorong Region, South Australia: significance and implications. *Sedimentology*, 52 (5), 987-1008.
- Zachariasse, W.J., Kontakiotis, G., Lourens, L.J. and Antonarakou, A.** (2021) The Messinian of Agios Myron (Crete, Greece): a key to better understanding of diatomite formation on Gavdos (south of Crete). *Palaeogeogr. Palaeoclimatol. Palaeoecol.*, 581, 110633.
- Zhang, F., Xu H., Konishi, H., Kemp, J.M., Roden, E.E. and Shen, Z.** (2012) Dissolved sulfide-catalyzed precipitation of disordered dolomite: Implications for the formation mechanisms of sedimentary dolomite. *Geochim. Cosmochim. Acta*, 97, 148-165.

Sample	Lithology	% Dolomite
13	Diatom-bearing mudstone	9.7
10	Diatomaceous shale	1.8
3	Dolomitic mudstone	61.1
2	Dolomitic mudstone	46.9

Table 1. Relative percentage of dolomite in the three lithologies. See Fig. 2 for details.

Sample	Lithology	$\delta^{13}\text{C}$	SD $\delta^{13}\text{C}$	$\delta^{18}\text{O}$	SD $\delta^{18}\text{O}$
8	Dolomitic mudstone	-4.8	0.02	+4.8	0.04
6	Dolomitic mudstone	-3.5	0.04	+3.4	0.03
5	Dolomitic mudstone	-5.4	0.03	+6.2	0.04
4	Dolomitic mudstone	-1.6	0.03	+5.7	0.04
3	Dolomitic mudstone	-0.9	0.03	+6.8	0.04
2	Dolomitic mudstone	-0.6	0.02	+4.6	0.03
Average value		-2.8		+4.4	

Table 2. $\delta^{13}\text{C}$ and $\delta^{18}\text{O}$ of dolomitic mudstones; SD = standard deviation. See Fig. 2 for details.

Lithology	Diatomaceous shale		Diatom-bearing mudstone	Dolomitic mudstone		
	10	12		13	8	3
Sample	10	12	13	8	3	2
% TOC	0.7	0.4	0.3	2.2	2.3	2.0
SC <i>n</i> -alcohols (C ₁₆₋₂₅)	5.9 (1.1)	12 (2.6)	9.4 (3.7)	0.9 (11.4)	3.8 (19.8)	2.0 (13.8)
LC <i>n</i> -alcohols (C ₂₆₋₃₄)	59.3 (11.6)	167.8 (35.8)	156.8 (61.9)	2.9 (35.1)	10.7 (55.4)	8.2 (56.5)
Sum <i>n</i> -alcohols (C ₁₆₋₃₄)	65.2 (12.7)	179.8 (38.4)	166.2 (65.6)	3.9 (46.4)	14.5 (75.3)	10.2 (70.3)
Archaeal lipids	0.0 (0.0)	0.0 (0.0)	0.0 (0.0)	1.3 (16.0)	0.6 (2.9)	0.3 (1.9)
Tetrahymanol	0.0 (0.0)	0.0 (0.0)	0.0 (0.0)	0.0 (0.0)	0.1 (0.5)	0.0 (0.3)
Sterols	73.2 (14.2)	81.8 (17.4)	15.4 (6.1)	0.4 (4.6)	1.2 (6.5)	0.6 (4.0)
1,X-diols	345.5 (67.2)	167.1 (35.6)	71.9 (28.3)	0.0 (0.0)	0.3 (1.4)	1.1 (7.8)
1,X-keto-ols	29.9 (5.8)	40.2 (8.6)	traces (0.0)	2.7 (33.0)	2.5 (13.1)	2.3 (15.5)
MAGE <i>n</i> -C _{16:0}	0.0 (0.0)	0.0 (0.0)	0.0 (0.0)	0.0 (0.0)	0.1 (0.5)	0.0 (0.2)
Sum lipid alcohol fraction	513.8	468.9	253.5	8.3	19.3	14.6

Table 3. Content of total organic carbon (TOC) and main biomarkers in the three lithologies studied. Lipid content is given in $\mu\text{g/g}$ TOC; percentage of a compound in the alcohol fraction provided in brackets; SC = short-chain; LC = long-chain; MAGE = monoalkyl glycerol ether. See Fig. 2 for details.

Lithology	Sedimentology and petrography	Mineralogical and element composition	Stable isotopes	TOC and biomarkers
Diatomaceous shale	<i>Finely laminated fabric</i> Abundant and well-preserved biosiliceous remains confined in biogenic laminae typified	Almost pure siliceous composition of diatom valves Low dolomite content (<i>ca</i> 2%)	–	TOC 0.4–0.7% Predominance of well-preserved algal-derived lipids

	by diatoms of the families Thalassionemataceae and Rhizosoleniaceae			
Diatom-bearing mudstone	<i>Laminated to massive fabric</i> Common and poorly-preserved biosiliceous remains closely associated with flaky clays	Diatom valves enriched in Al, Fe, K and Mg, mimicking the composition of flaky clays closely associated with dolomite crystals in the dolomitic mudstone More abundant dolomite content (<i>ca</i> 10%)	–	TOC 0.3% Predominance of well-preserved algal-derived lipids
Dolomitic mudstone	<i>Laminated to massive fabric</i> Rare and very poorly-preserved biosiliceous remains interspersed in a dolomite-rich and flaky clay-rich matrix Cauliflower to globular hollow dolomite crystals Pyrite framboids	Flaky clays closely associated with dolomite crystals are enriched in Fe, K and Mg Abundant dolomite content (up to <i>ca</i> 60%)	$\delta^{13}\text{C}$ average value: -2.8 $\delta^{18}\text{O}$ average value: +4.4	TOC 2.0–2.3% Occurrence of degraded algal lipids Tetrahymanol MAGs

Table 4. Overview of main features of the three lithologies; TOC = total organic carbon.

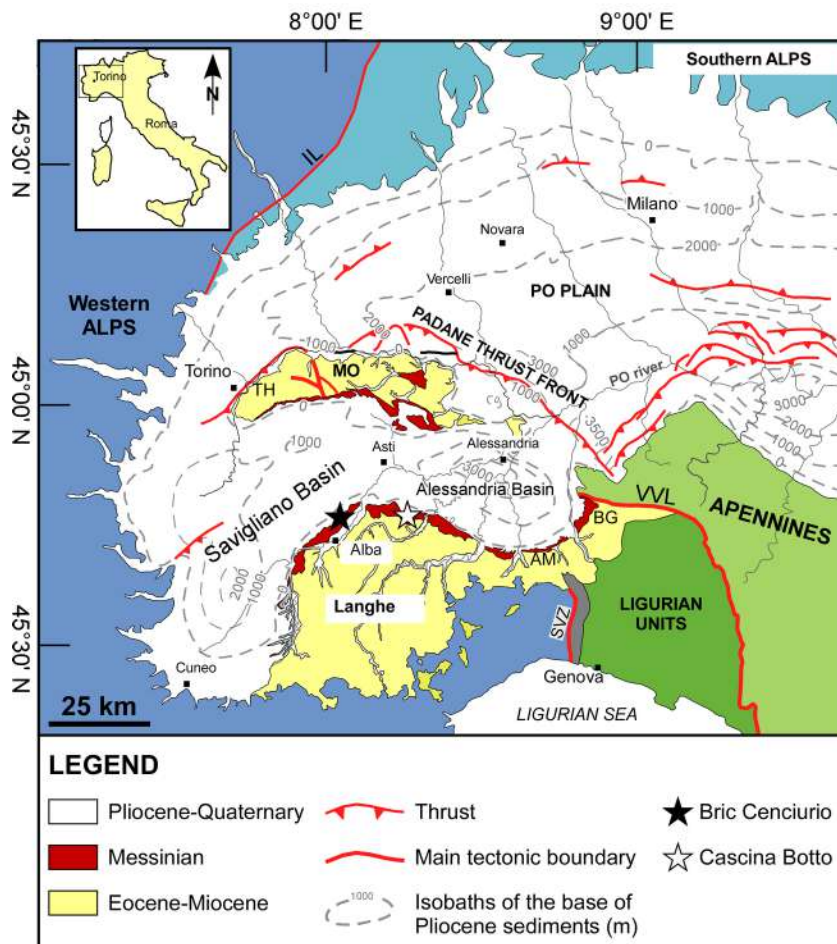


Fig. 1 - Two thirds page width

SED_13053_Figure 1.tif

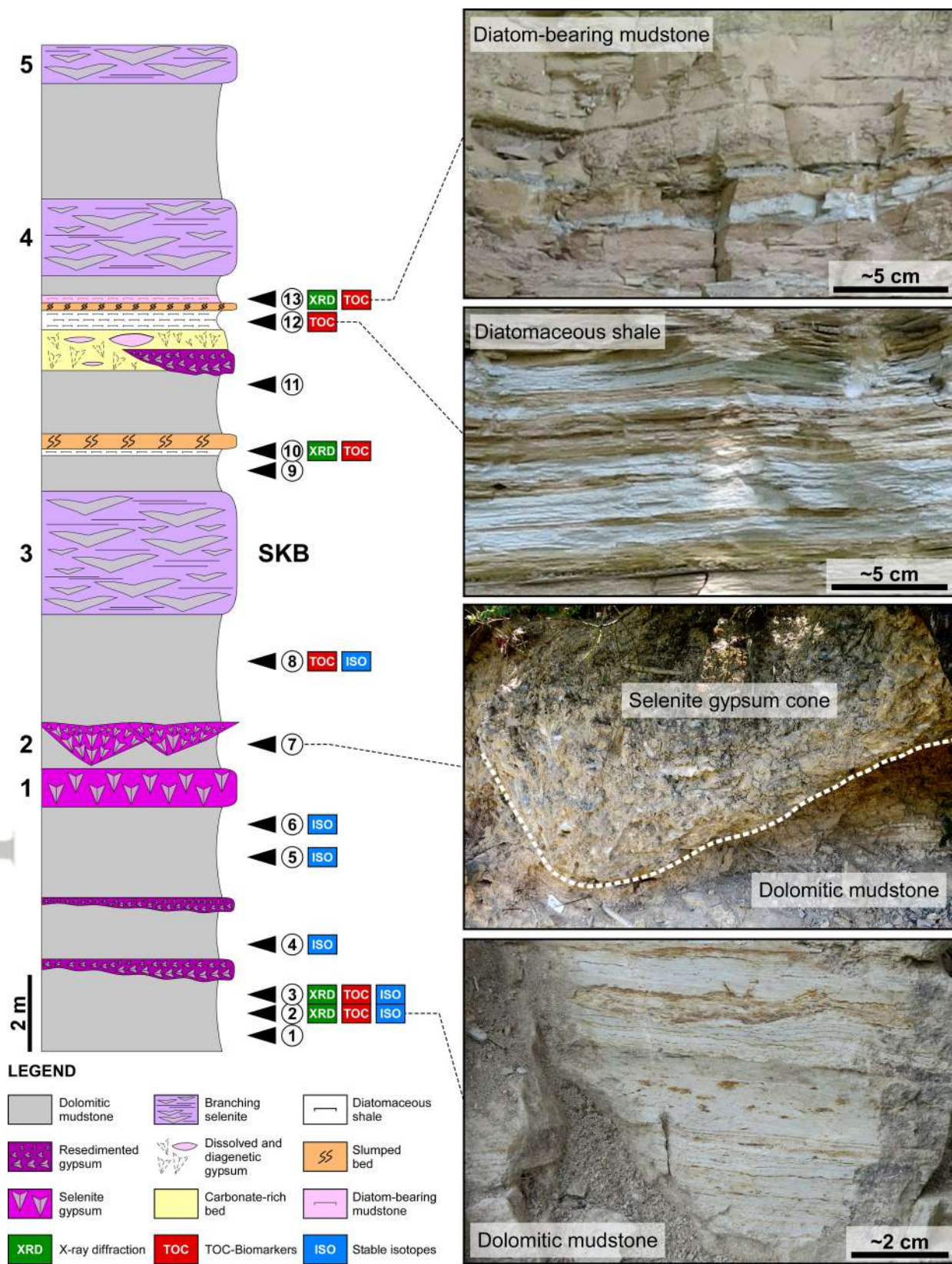


Fig. 2 - 1 page width

SED_13053_Figure 2.tif

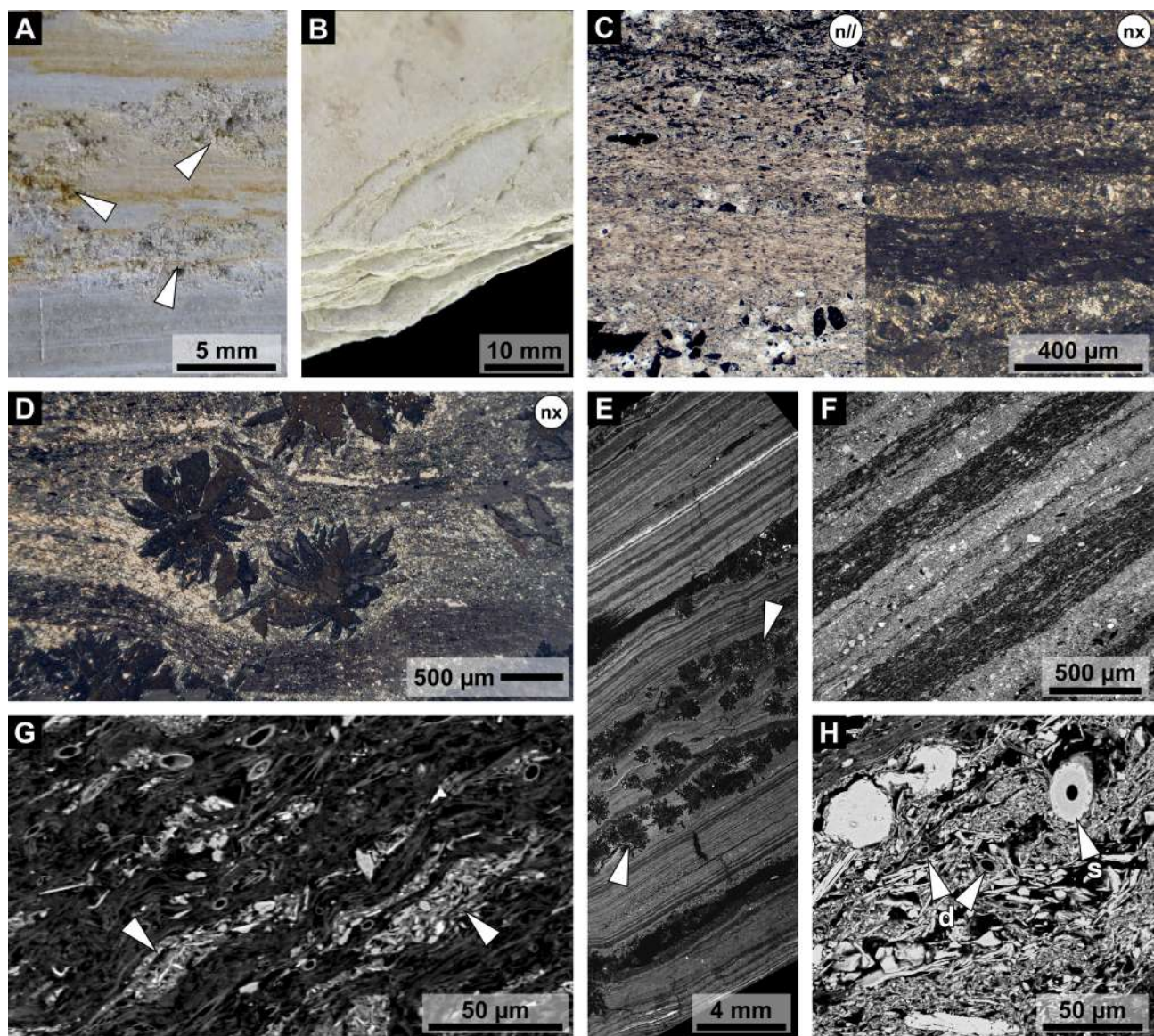


Fig. 3 - 1 page width

SED_13053_Figure 3.tif

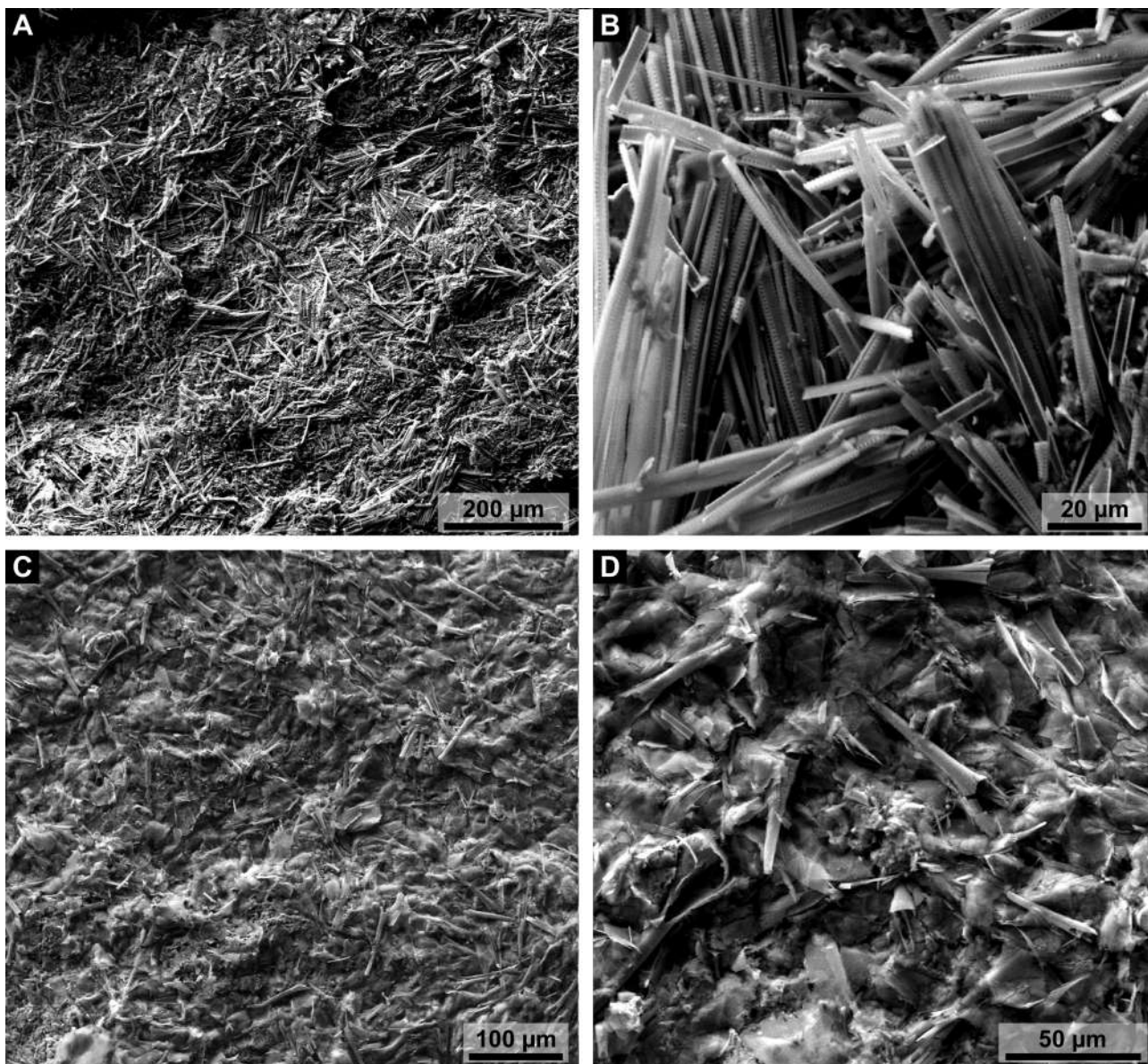


Fig. 4 - 1 page width

SED_13053_Figure 4.tif

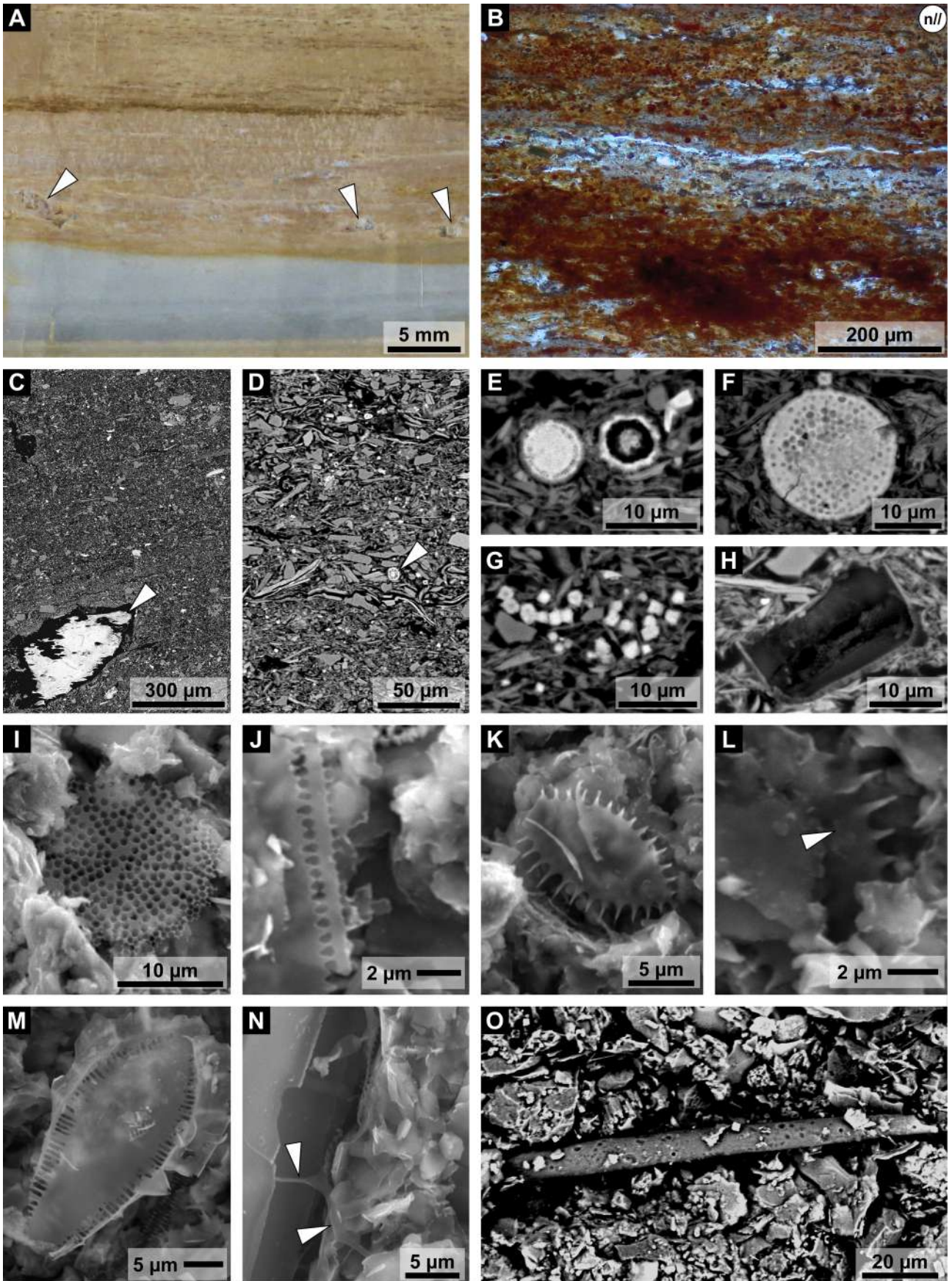


Fig. 5 - 1 page width

SED_13053_Figure 5.tif

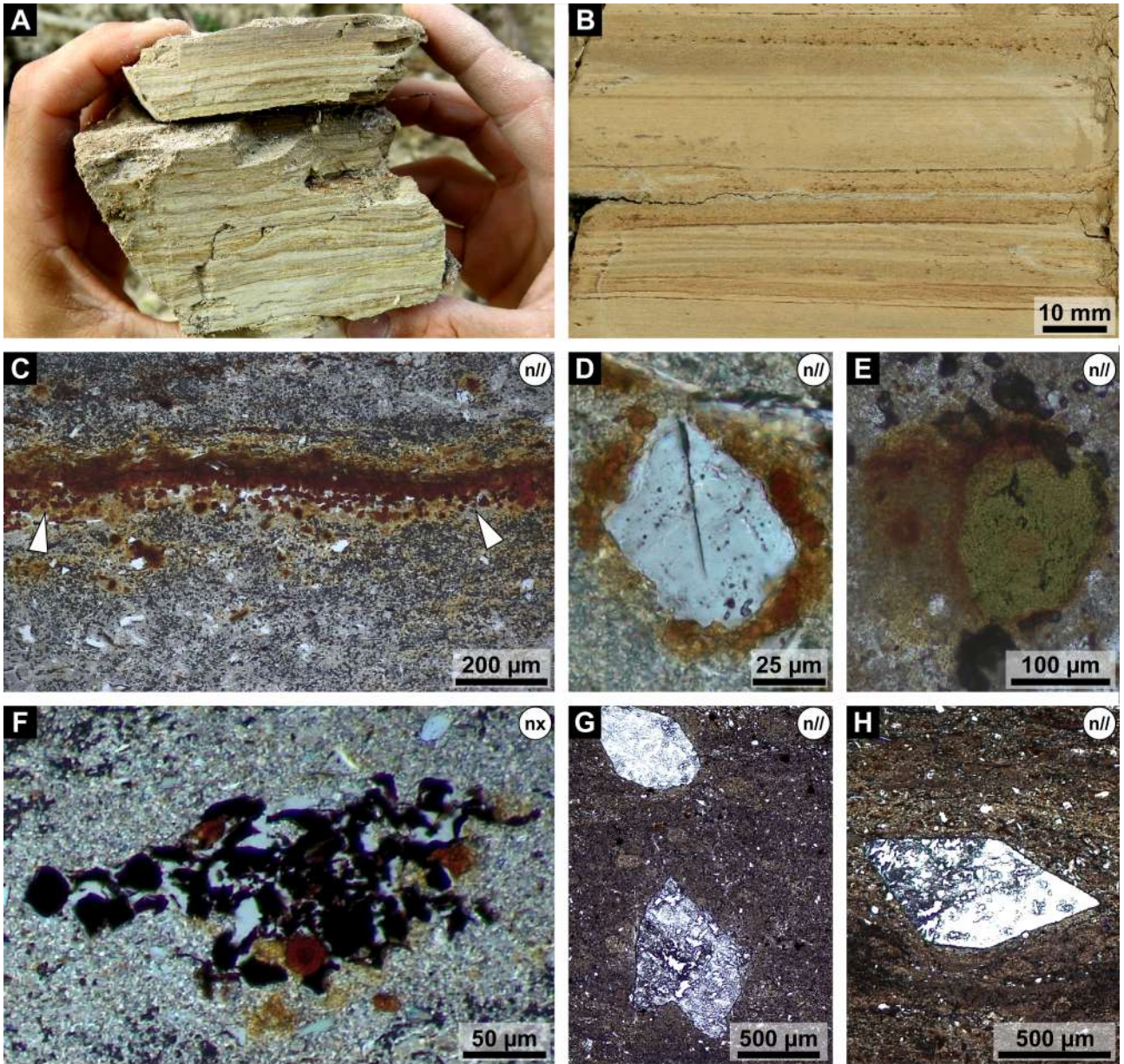


Fig. 6 - 1 page width

SED_13053_Figure 6.tif

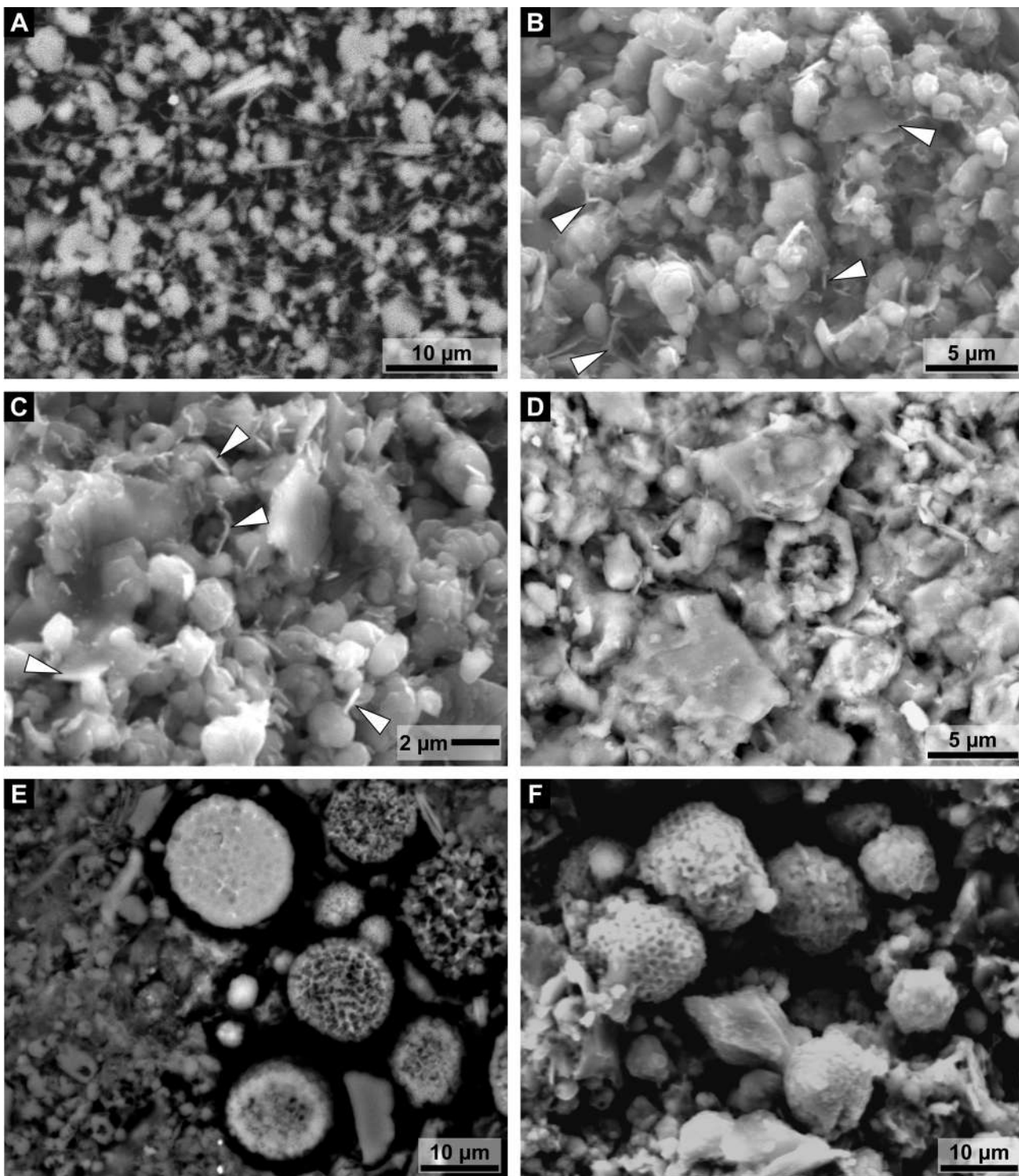


Fig. 7 - 1 page width

SED_13053_Figure 7.tif

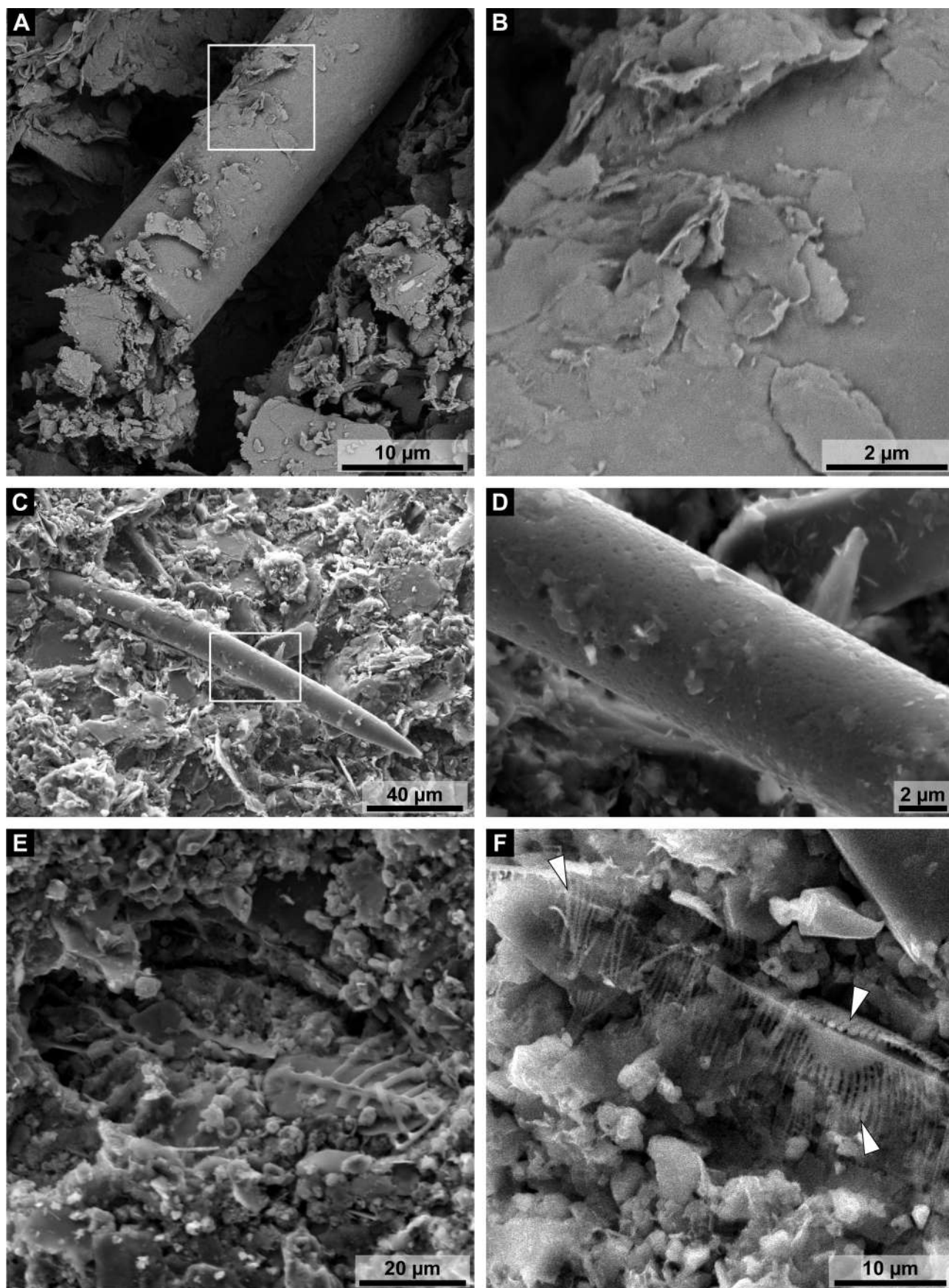


Fig. 8 - 1 page width

SED_13053_Figure 8.tif

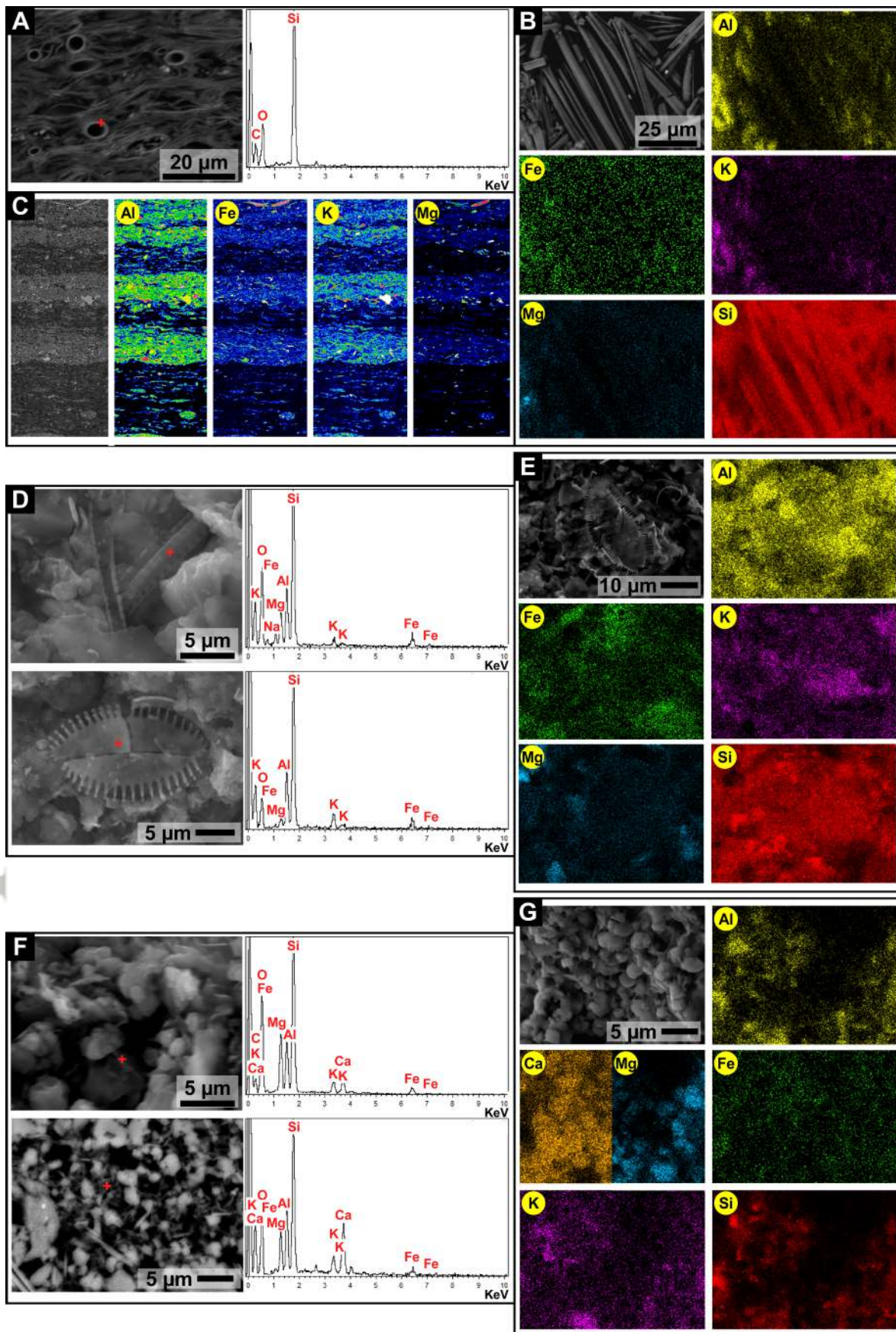


Fig. 9 - 1 page width

SED_13053_Figure 9.tif

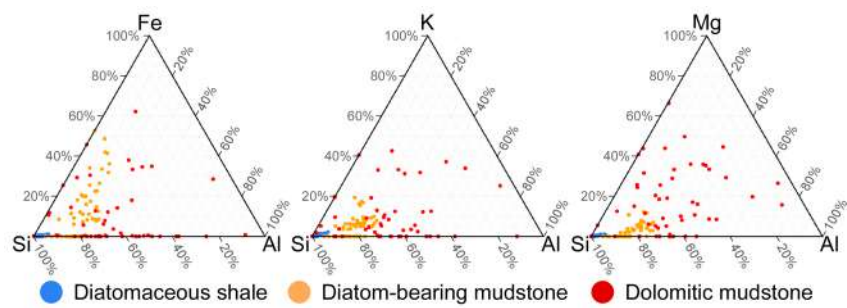


Fig. 10 - Two thirds page width
SED_13053_Figure 10_modified_2ndversion_highres.tif

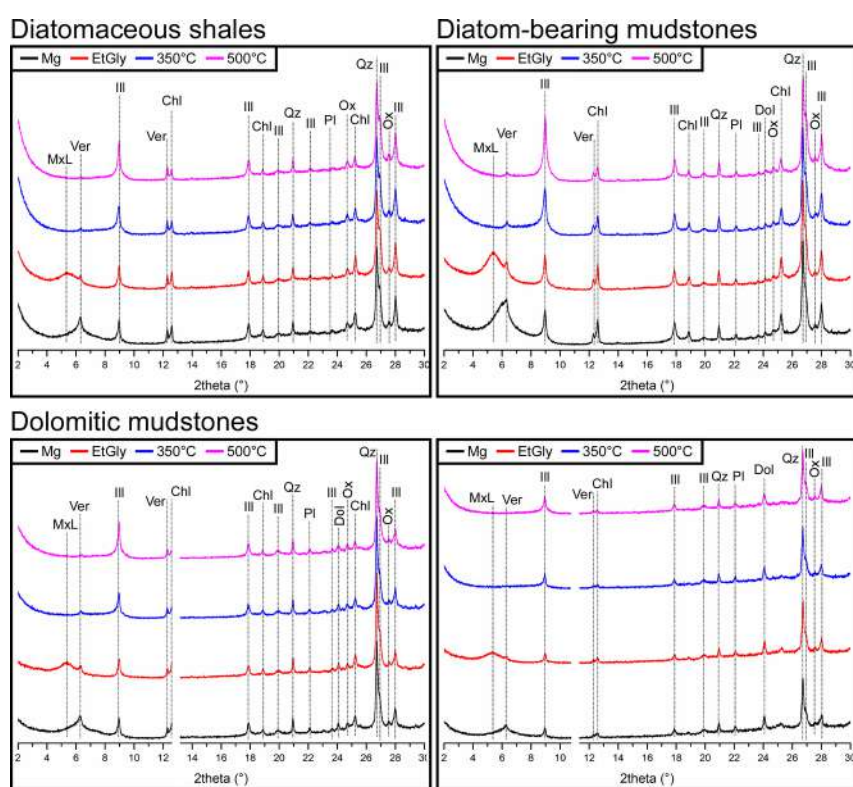


Fig. 11_modified - Two thirds page width

SED_13053_Figure 11_modified_2ndversion_highres.tif

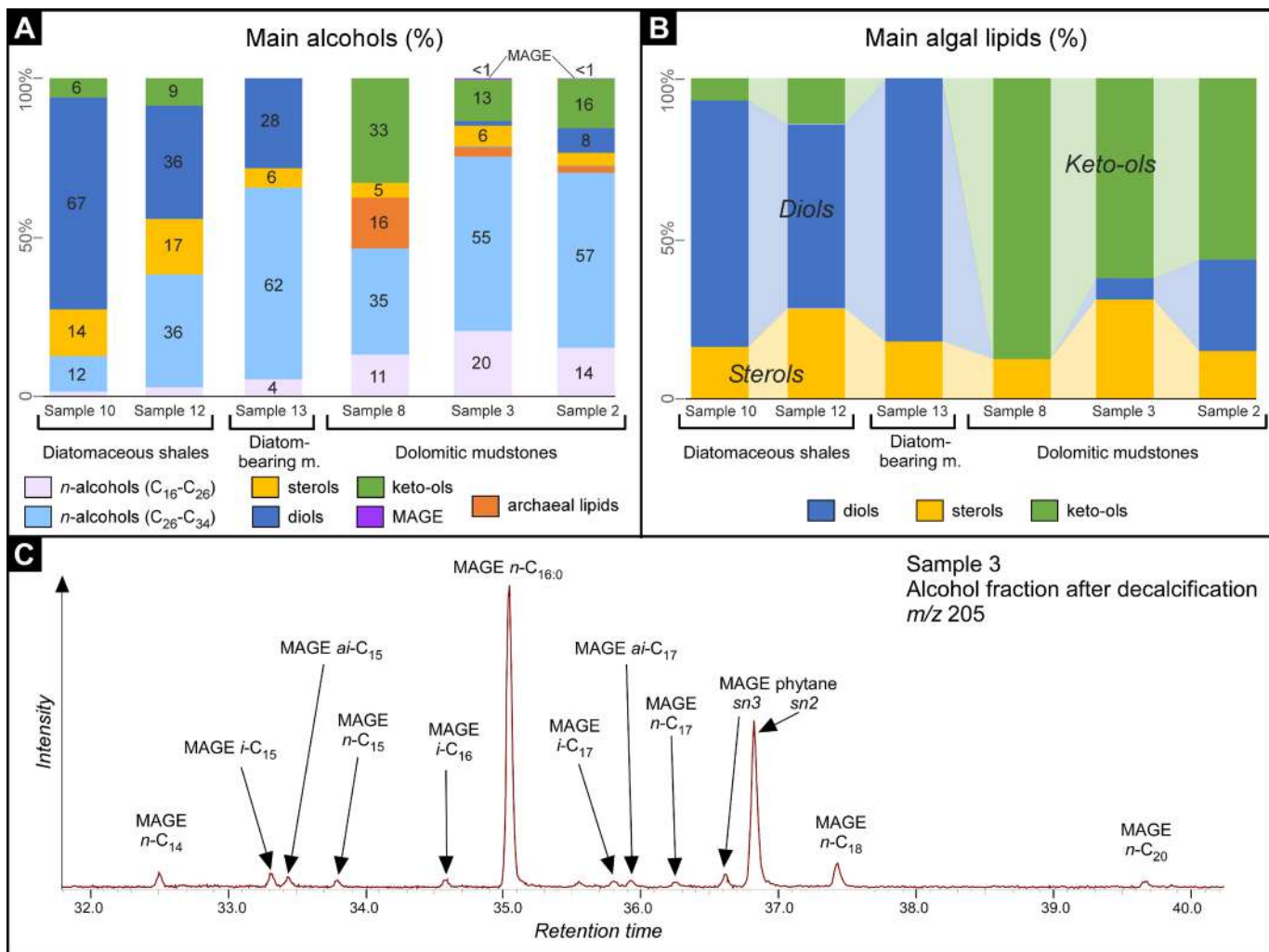


Fig. 12_modified - 1 page width

SED_13053_Figure 12_modified.tif

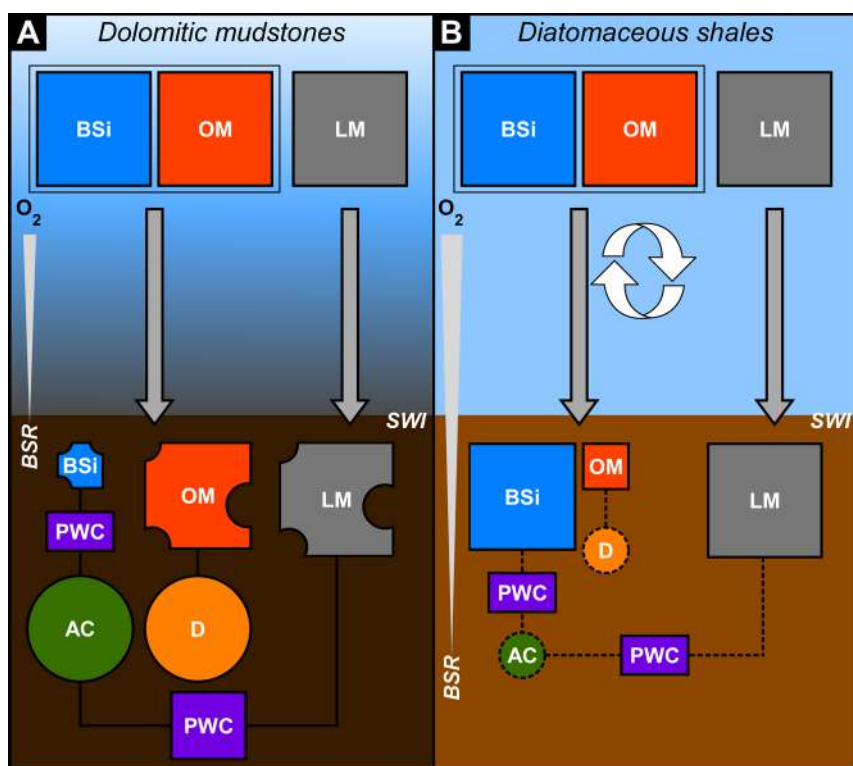


Fig. 13_modified - Two thirds page width
 SED_13053_Figure 13_modified.tif